



# Assimilating Geostationary Satellite Visible Reflectance Data: developing and testing the GSI-EnKF-CRTM-Vis technique

Chong Luo<sup>1,2</sup>, Yongbo Zhou<sup>1,2</sup>, Yubao Liu<sup>3,4</sup>, Wei Han<sup>5</sup>, Bin Yao<sup>6</sup>, and Chao Liu<sup>1,2,\*</sup>

- <sup>1</sup>State Key Laboratory of Climate System Prediction and Risk Management, Nanjing University of Information Science and Technology, Nanjing 210044, China
- <sup>2</sup>China Meteorological Administration Aerosol-Cloud-Precipitation Key Laboratory, School of Atmospheric Physics, Nanjing University of Information Science and Technology, Nanjing 210044, China
- <sup>3</sup>Precision Regional Earth Modeling and Information Center, Nanjing University of Information Science and Technology, Nanjing 210044, China
- 4 Collaborative Innovation Center on Forecast and Evaluation of Meteorological Disasters, Nanjing University of Information Science and Technology, Nanjing, 210044, China
  - <sup>5</sup>CMA Earth System Modeling and Prediction Centre, Beijing, China
  - <sup>6</sup>Key Laboratory of Transportation Meteorology of China Meteorological Administration, Nanjing Joint Institute for Atmospheric Sciences, Nanjing, China
- 15 Correspondence to: Chao Liu (chao liu@nuist.edu.cn)

**Abstract.** Satellite visible reflectance observations in cloud- and precipitation-affected regions contain substantial information on weather systems, while data assimilation (DA) of visible data is still challenging due to the complexity of forward operators and the non-Gaussian distribution of cloud variables. This study developed an interface within the framework of the popular Gridpoint Statistical Interpolation (GSI) system to assimilate synthetic visible reflectance simulated by Community Radiative Transfer Model (CRTM). The interface employed a spatial interpolation to ensure accurate alignment between model grids and satellite data, and also facilitating a bidirectional mapping between the state variable space and the observation space. The key implementations within the newly developed GSI-EnKF-CRTM-Vis DA technique include integrating a new observation type from geostationary visible imager, incorporating the module for simulating visible reflectance in CRTM, and extending cloud-related control variables. We employed an ensemble-based DA framework in which ensemble members were initialized with multiple physical parameterization schemes, thereby better representing the ensemble spread arising from cloud parameterization differences. The performance of the GSI-EnKF-CRTM-Vis, configured with the Ensemble Square Root Filter (ENSRF) algorithm, was evaluated by assimilating the Himawari-8 Advanced Himawari Imager (AHI) 0.64 µm visible reflectance for a heavy rainfall event over East Asia on 21 September 2024 under the framework of Observing System Simulation Experiment (OSSE). The experimental results demonstrated that DA of visible reflectance effectively corrected the overestimated cloud water path (CWP), reducing the mean absolute error by 1.5 % on average with forecast improvements lasting 6 hours. Probability density function analysis confirmed significant correction of thin clouds (with reflectance less than 0.2 and CWP less than 0.1 kg·m<sup>-2</sup>). DA of visible reflectance improved the spatial extent of light precipitation, as is evidenced by the improved Equitable Threat Score (ETS) across thresholds (except the 0.1 mm threshold) and the reduced False Alarm Rate (FAR). For the U- and V-component winds, temperature, water vapor mixing ratio, DA of visible reflectance generated





negligible adjustments as visible reflectance data are insensitive to these non-cloud variables. The newly developed GSI-EnKF-CRTM-Vis DA technique facilitates the ensemble-based DA of satellite visible reflectance with ensemble members initialized with multiple physical parameterization schemes.

## 1 Introduction

50

60

Satellite data offers wide coverage, high spatiotemporal resolution, and good stability and consistency. It constitutes over 90 % of observations in data assimilation (DA) systems and plays an important role in the global observation system (Bauer et al., 2010, 2015; Zhu et al., 2016). Significant efforts have been devoted to assimilating all-sky infrared (IR) and microwave (MW) radiances. All-sky IR DA has been shown to improve cloud analysis, deep convection representation, upper-tropospheric temperature, moisture, and lower-tropospheric wind fields (Otkin et al., 2010, 2012; Okamoto, 2012; Stengel et al., 2013; Geer et al., 2019), as well as forecasts of tropical cyclone and warm-sector heavy rainfall (Honda et al., 2018; Lou et al., 2024). Similarly, all-sky MW radiance DA improves humidity, pressure, wind analyses (Geer et al., 2010; Migliorini et al., 2019; Ma et al., 2022), leading to better forecasts of typhoon track, intensity, and precipitation (Chambon et al., 2017; Chen et al., 2023; Xu et al., 2024). Nonetheless, persistent limitations remain: geostationary satellites lack MW instruments, and polar orbiting platforms cannot provide the spatiotemporal resolution required for convective scale DA (Schröttle et al., 2020). IR channels are predominantly sensitive to high-level clouds, limiting their ability to detect lower-level cloud structures and often obscuring hydrometeor layers beneath thick ice clouds (Platnick et al., 2003).

The DA of visible (VIS) reflectance remains challenging due to the complexity of forward operators and the non-Gaussian nature of cloud fields (Bonavita et al., 2018; Zhou et al., 2023). Nevertheless, compared to IR and MW observations, assimilating VIS reflectance data offers distinct advantages. VIS reflectance data has better penetration capability than the IR observations, enabling them to reflect in-cloud microphysical properties (Twomey, 1977; Nakajima and King, 1990). VIS reflectance is much more sensitive to cloud properties than the conventional non-cloud atmospheric variables, facilitating effective separation of cloud signals (Zhou et al., 2022). Secondly, the strong brightness contrast between clouds and the surface in VIS channels allows clear identification of low-level clouds (Heinze et al., 2017; Scheck et al., 2020). Additionally, VIS reflectance typically offers higher temporal and spatial resolution (Yang et al., 2017) than the MW radiance. This proves highly valuable for improving forecasts of rapidly evolving convective weather systems. Therefore, DA of VIS reflectance holds significant potential (Polkinghorne et al., 2011).

To date, researchers and operational agencies have explored the DA of VIS radiance, incorporating it into DA systems using both variational (VAR) and ensemble DA methods. For example, Vukicevic et al. (2004) assimilated GEOS-9 VIS radiance into the Regional Atmospheric Modeling and Data Assimilation System (RAMDAS) using the four-dimensional (4D) VAR method. The VIS radiance positively impacted the model's cloud field forecasts. However, the VAR methods face challenges for all-sky DA. They rely on linearized adjoint models, which can lead to significant errors under strongly nonlinear cloud conditions (Errico et al., 2007; Lopez, 2007). Additionally, the static background error covariance matrix in VAR



85

95

100



methods struggles to capture the rapid spatiotemporal variations of clouds and precipitation. Consequently, it fails to adequately represent the error characteristics associated with clouds and precipitation (Zhang et al., 2013; Lei et al., 2021). In contrast, ensemble DA methods directly simulate nonlinear processes via Monte Carlo sampling, avoiding linear approximations (Houtekamer and Zhang, 2016). Moreover, they dynamically estimate background error covariance from ensemble forecasts. This incorporates valuable flow-dependent information. Consequently, ensemble DA methods show greater potential than VAR methods for assimilating VIS radiance in cloud regions.

Scheck et al. (2020) conducted a case study in which visible radiance data from the Spinning Enhanced Visible and Infrared Imager (SEVIRI) on Meteosat-10 was assimilated into the Kilometre-scale ENsemble Data Assimilation (KENDA) system, employing the Local Ensemble Transform Kalman Filter (LETKF) method. The results demonstrated significant improvements in cloud cover, significant benefits for humidity and temperature fields, and a positive impact on precipitation forecasts. Zhou et al. (2022) evaluated the Data Assimilation Research Testbed (DART)-Radiative Transfer for TOVS (RTTOV) system by assimilating the Fengyun-4A Advanced Geostationary Radiation Imager (AGRI) VIS radiance data. They compared two filter methods, the Ensemble Adjustment Kalman Filter (EAKF) and the Rank Histogram Filter (RHF). The comparison showed improvements in cloud variables and precipitation rates, along with a slight positive impact on non-cloud variables. Further improvements were achieved by employing a localized particle filter (Poterjoy, 2016), which effectively addressed the non-Gaussian problems during the DA processes (Zhou et al., 2023). Kugler et al. (2023) employed the EAKF method within an Observing System Simulation Experiment (OSSE) framework to assimilate VIS radiance into a convective-scale system. Observations were simulated using the RTTOV configured with the Method for Fast Satellite Image Synthesis (MFASIS). The results suggested improved precipitation and cloud cover forecasts.

The performance of ensemble-based DA is mostly sensitive to the ensemble spread of ensemble members. There are two primary approaches to initialize ensemble forecasts for ensemble DA methods. One is adding perturbations to initial fields, and the other utilizes different physical parameterization schemes. While operational systems commonly employ the initial-field perturbation method for its computational efficiency, this approach poses a significant problem for the DA of VIS reflectance. Since all ensemble members typically share the same physical parameterization scheme, they generate a low spread in cloud-related variables. This insufficient dispersion fails to represent the true uncertainty in cloud properties. In contrast, the multi-physics approach better characterizes ensemble spread from cloud parameterization differences (Stensrud et al., 2000). This capability is particularly critical for VIS reflectance DA. Since VIS reflectance is highly sensitive to parameters such as cloud optical thickness, effective particle radius, and phase state.

Therefore, we enhanced the existing GSI-EnKF DA system by implementing a new interface to support DA of VIS reflectance from the geostationary satellites. This development resulted in a DA technique capable of initializing ensemble forecasts using multiple physical parameterization schemes and enabling all-sky DA of VIS reflectance. To verify the effectiveness of the newly developed GSI-EnKF-CRTM-Vis DA technique, we conducted an OSSE by assimilating Himawari-8 Advanced Himawari Imager (AHI) visible reflectance data for a convective event. Specifically, we assimilated the AHI Channel 3 (centering at 0.64 µm) VIS reflectance simulated by the Community Radiative Transfer Model (CRTM). We



105

110

115

120

125

130



employed the Ensemble Square Root Filter (ENSRF) as the DA method and used the heavy rainfall event over East Asia on 21 September 2024 as a representative case for detailed analysis. The remainder of this paper is organized as follows: Sect. 2 details the key modifications implemented within the GSI-EnKF-CRTM-Vis DA technique to assimilate Himawari-8 AHI VIS reflectance data, and the experimental design, including model configurations, ensemble setup, and evaluation metrics. Sect. 3 discusses the results from single-observation and cycled DA experiments, and Sect. 4 summarizes the conclusions.

## 2 DA system and experiment designs

## 2.1 Development of the GSI-EnKF-CRTM-Vis DA technique

The GSI DA system was developed by the National Centers for Environmental Prediction (NCEP) under the National Oceanic and Atmospheric Administration (NOAA). This system integrates variational methods, EnKF, and hybrid DA techniques. It employs physical space interpolation for efficient parallel computing and offers multi-scheme DA capabilities, supporting real-time mesoscale analysis and rapid-update cycling (Wen et al., 2017). This study used GSI v3.7 and EnKF v1.3 as the experimental platform. The GSI-EnKF system comprises two core components: the GSI Observer and the EnKF. The GSI Observer module is mainly responsible for the forward simulation of observations. The EnKF module comprises the core DA algorithm. It processes the differences between actual observations and those simulated by the CRTM forward operator in the Observer module, and calculates the analysis increments used to update the model state variables based on the flow-dependent background error covariance estimated from the ensemble members.

The standard GSI system lacks the capability to assimilate VIS reflectance data from the geostationary satellites, primarily due to the absence of the interface for processing VIS observations, the module of radiative transfer simulation for simulating VIS reflectance, and cloud-related control variables. To address these limitations, we developed the GSI-EnKF-CRTM-Vis DA technique to enable all-sky DA of visible reflectance data from Himawari-8 AHI. The key implementations of this technique are showed in Fig. 1.

Configuring observation type and forward operator in the GSI Observer module involves defining a new observation type named AHI\_VIS and integrating it into the GSI observation input interface (implemented in read\_ahi.f90 and read\_obs.f90 as shown in Fig. 1). Read\_obs.f90 serves as the main dispatch routine for reading various types of observation data. It identifies the observation type from the input BUFR files and calls the appropriate subroutines for each sensor. We added the subroutine to identify the new observation type of AHI\_VIS, when an observation of type AHI\_VIS is encountered, it invokes the subroutine read\_ahi.f90 to handle the specific data reading and preprocessing. The module of reading visible reflectance data and sun-satellite viewing geometries from the Himawari-8 AHI was implemented in read\_ahi.f90. Additionally, this subroutine performs preliminary quality control, for instance, excluding invalid observation points where the reflectance value exceeds 1 or falls below 0. When processing observations of type AHI\_VIS, the corresponding CRTM forward operator for AHI is directly invoked. This operator uses atmospheric data from the background field to simulate the VIS reflectance image.



140



To support the forward simulation, we employed CRTM v2.1.3 to serve as the forward observation operator, loading the AHI visible transmittance coefficient dataset (.bin files). This version was selected primarily due to its robust compatibility and proven stability within our operational environment, which ensured reliable and consistent radiative transfer simulations. Key subroutines for the forward simulation were implemented in crtm\_interface.f90 and setuprad.f90 (Fig. 1). Setuprad.f90 is mainly responsible for the initialization configuration of forward simulation and the setting of input parameters, which was modified by developing module to prepare input parameters for CRTM simulation. It invokes crtm\_interface.f90, which serves as the main program for radiative transfer simulation within CRTM, executing the radiative transfer processes to simulate visible reflectance. Therefore, we implemented the subroutine to enable simulate AHI visible reflectance in crtm\_inerface.f90. To ensure physical consistency and eliminate forward operator errors originating from inconsistent cloud property, the calculation methods for cloud parameters, including cloud water path (CWP), effective particle radius, and phase state, were configured to be identical to those used to generate the simulated observations.

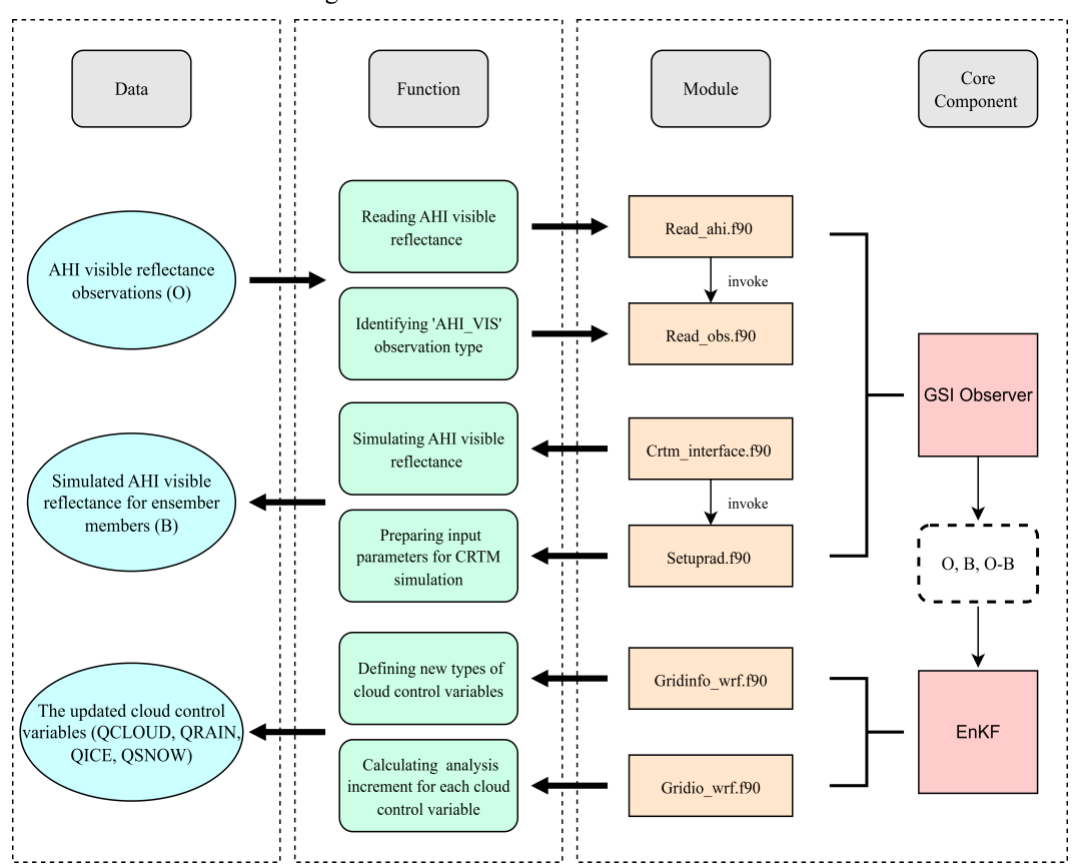


Figure 1: The workflow and major modifications within GSI-EnKF-CRTM-Vis for Himawari-8 AHI visible reflectance assimilation.

The control variables of VIS reflectance data DA must include not only conventional atmospheric variables, but also the mass mixing ratios of hydrometeors in clouds (including cloud water, ice crystals, rainwater, and snow). These variables were selected because they represent the common core hydrometeors consistently present across the diverse physical



155

160

170



parameterization schemes used to generate our ensemble members. By focusing on this maximal intersection set, we ensured the control variables were available and physically meaningful for all ensemble forecasts. However, the standard GSI-EnKF system does not incorporate these cloud microphysical variables into its control variable set (default: U- and V-component winds, surface pressure, virtual temperature, specific humidity). To address this limitation, we modified the source code of key modules, including gridinfo\_wrf.f90 and gridio\_wrf.f90 (Fig. 1). Specifically, the gridinfo\_wrf.f90 module is responsible for defining the types of control variables, therefore we introduced the new type including cloud water mixing ratio (ql), ice mixing ratio (qi), rainwater mixing ratio (qr), and snow mixing ratio (qs) to incorporate them into the EnSRF control variables. The gridio\_wrf.f90 module handles the computation of analysis increments for each control variable during the DA process. Correspondingly, we developed the incremental calculation subroutines for each cloud control variable.

## 2.2 Configurations of the GSI-EnKF-CRTM-Vis DA technique

### 2.2.1 The CRTM forward operator

Simulating a Himawari-8 AHI VIS imagery using CRTM requires atmospheric variable profiles (pressure, temperature, etc.), surface parameters (surface type, surface temperature, etc.), sun-satellite viewing geometries, and cloud parameters (the vertical structures of cloud phase, effective particle radius and CWP). The sun-viewing geometries (i.e., solar zenith and azimuth angles, satellite zenith and azimuth angles) were derived from AHI GEO data. Cloud-related input parameters are computed using the formulas below.

According to Eq. (1) in Thompson et al. (2004), the effective radius of water, rain, snow, and graupel particles can be estimated as:

$$R_{x} = \frac{1}{2} \times \left(\frac{6\rho_{o}q_{x}}{\pi\rho_{x}N_{x}}\right)^{\frac{1}{k}},\tag{1}$$

where R denotes the effective radius, and the subscript x represents the particle type.  $\rho_o$  and  $\rho_x$  are the air density and particle density, respectively.  $N_x$  is the particle concentration,  $q_x$  is the mass mixing ratio, and k is a constant. The particle densities  $\rho_x$  are: 1000 for water, 1000 for rain, 100 for snow, and 500 kg·m<sup>-3</sup> for graupel. The concentrations  $N_x$  are: 300, 48, 6, and 24 cm<sup>-3</sup>, respectively. The constants k are: 3, 3, 2.4, and 3, respectively.

The effective radius for ice particles is calculated using the formulas from Hong et al. (2004) and Yao et al. (2018):

$$N_i = \min(\max(c \cdot (\rho_o \cdot \max(q_i, 10^{-15}))^d, 10^3), 10^6), \tag{2}$$

$$M_i = \frac{\rho_o q_i}{N_i},\tag{3}$$

$$R_i = min\left(11.9 \times 0.75 \times 0.163 \times M_i^{\frac{1}{2}}, 500 \times 10^{-6}\right),\tag{4}$$





where  $N_i$  is the ice crystal concentration,  $c = 5.38 \times 107$ , d = 0.75,  $q_i$  is the ice mass mixing ratio, and  $M_i$  is the mass concentration per ice crystal.

According to Stephens (1978), the x water path for different hydrometeors over N atmospheric layers is computed as:

$$CWPx = \int \rho q_x \, dz = \sum_{k=1}^{N} (\rho_k \cdot q_{x,k} \cdot \Delta z_k), \tag{5}$$

In discrete form, the contribution from a single layer is:

$$\Delta CWPx, k = \rho_k \cdot q_{x,k} \cdot \Delta z_k , \tag{6}$$

where  $\rho$  is the air density,  $q_x$  is the hydrometeor mass mixing ratio, k is the vertical layer index, and  $\Delta z_k$  is the thickness of the kth layer.  $\rho_k$  and  $q_{x,k}$  denote the values at the k-th layer, respectively.

Sensitivity tests are essential to ensure physical plausibility of simulated observations before DA. VIS reflectance depends critically on cloud particle scattering properties and shows high sensitivity to CWP. Fig. 2 demonstrates a nonlinear reflectance–CWP relationship for AHI Channel 3. Smaller effective radii in water clouds increase REF sensitivity to CWP by enhancing scattering cross-section per unit mass. At identical particle sizes, ice clouds show higher reflectance than water clouds, attributed to stronger forward scattering and superior multiple-scattering efficiency of non-spherical ice crystals (Takano and Liou,1989; King et al., 2004). Increased solar zenith angle (Fig. 2b) reduces overall REF and weakens CWP sensitivity by lengthening optical paths and raising photon escape probability. reflectance consistently approaches saturation at CWP  $\approx 10 \text{ kg} \cdot \text{m}^{-2}$ .

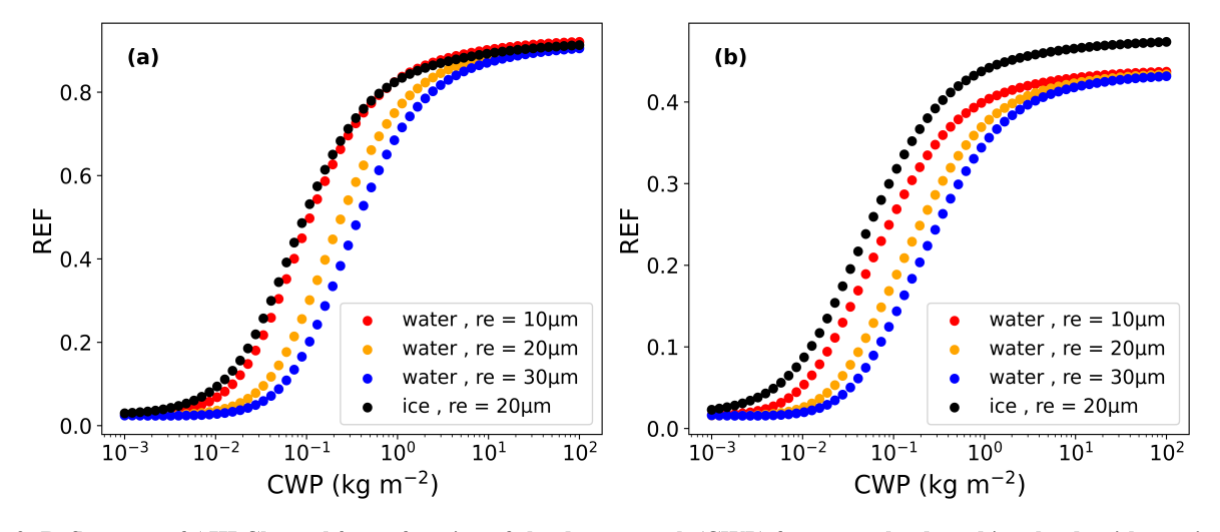


Figure 2: Reflectance of AHI Channel 3 as a function of cloud water path (CWP) for water clouds and ice clouds with varying effective radii. (a) Solar zenith angle =  $25^{\circ}$ , (b) Sensor zenith angle =  $60^{\circ}$ . Satellite zenith angle and relative azimuth angle are set to  $40^{\circ}$  and  $0^{\circ}$ , respectively.

180



195

200

205

210

215



To evaluate the capability of the CRTM to simulate AHI VIS imagery using the calculation formulas described above, we conducted a case study of Typhoon Doksuri (2023). This typhoon was selected due to its well-defined and complex cloud structures, which provide a rigorous test for the forward operator under extreme conditions. Simulations were performed at 00:00 UTC on 25 July 2023, corresponding to the typhoon's mature stage. The input parameters for the CRTM simulation, including atmospheric profiles, hydrometeor profiles, and surface properties, were derived from WRF simulation outputs. As shown in Fig. 3a–c, the simulated VIS imagery, CWP distribution, and solar zenith angle distribution are presented respectively. A strong correspondence is observed between cloud areas and the CWP distribution. Notably, the simulation clearly captured the typhoon's eye. Around the typhoon center, the solar zenith angle ranged from 55° to 60°, consistent with the scenario presented in Fig. 2b. Furthermore, the maximum simulated reflectance agreed well with Fig. 2b. These results confirmed that the CRTM forward operator and its associated algorithms are suitable for this OSSE.

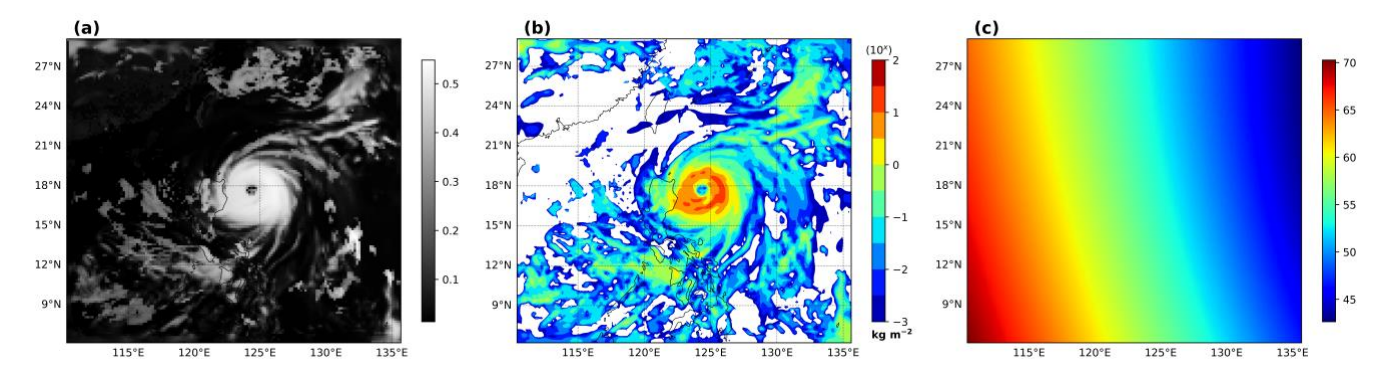


Figure 3: (a) Synthetic AHI Channel 3 (0.64  $\mu$ m) visible image for the Typhoon Doksuri (2023) at 00:00 UTC on 25 July 2023. The simulation is performed by CRTM with the inputs derived from the WRF simulations; (b) Cloud water path (CWP) distribution; (c) Solar zenith angle distribution.

#### 2.2.2 The WRF model for ensemble forecasts

This study focuses on a band-shaped convective precipitation event over East Asia. The event occurred from September 21 to 22, 2024, within approximately 110° E–135° E, 20° N–40° N. It extended northeast-to-southwest, impacting China's southeastern coast, the Korean Peninsula, and the Japanese archipelago. We conducted an OSSE using the Advanced Research WRF (ARW) model version 4.1.5. OSSEs offer a key advantage: they allow quantitative assessment of new observing systems' impact on forecasts within a controlled environment where the "truth" (Nature Run) is known (Arnold and Dey, 1986; Chen et al., 2024). The complete framework comprises three core components: the nature run, the DA experiment (EXP), and the control experiment (CTRL).

(1) Nature run, represents the true state. This study employed ECMWF Reanalysis v5 (ERA5) reanalysis data as the nature run. ERA5 performs well in simulating heavy rainfall and extreme precipitation events (Hersbach et al., 2020). Its configuration includes 1 hour temporal resolution,  $0.25^{\circ} \times 0.25^{\circ}$  horizontal resolution, and 37 vertical levels.



225



- (2) The EXP contained 40 ensemble members, generated by combining different physical parameterization schemes (Table 1: 6 microphysics, 5 cumulus, 2 planetary boundary layer (PBL) schemes). To enhance initial ensemble spread, we deliberately varied the spin-up times for the members in increments of 12 hours, resulting in: 26h, 38h, 50h, 62h, 74h, 86h, and 98h. All members used the same schemes for: RRTM longwave radiation, Dudhia shortwave radiation, Monin-Obukhov surface layer, and Thermal Diffusion land surface.
- (3) The CTRL, serving as the DA benchmark. It was a single-member experiment with identical configuration (physical parameterization schemes and spin-up time) to the first member of the EXP but performed no DA.

All experiments were operated within the domain shown in Fig. 4 (199 × 199 grid points, 15 km horizontal resolution, 50 vertical layers with 50 hPa model top). We extracted initial conditions (ICs) and lateral boundary conditions (LBCs) for both CTRL and EXP from 0.25° × 0.25° Global Forecast System (GFS) forecast data. Comparative analysis of CTRL and EXP results will evaluate the impact VIS reflectance DA on cloud fields and heavy rainfall forecast performance.

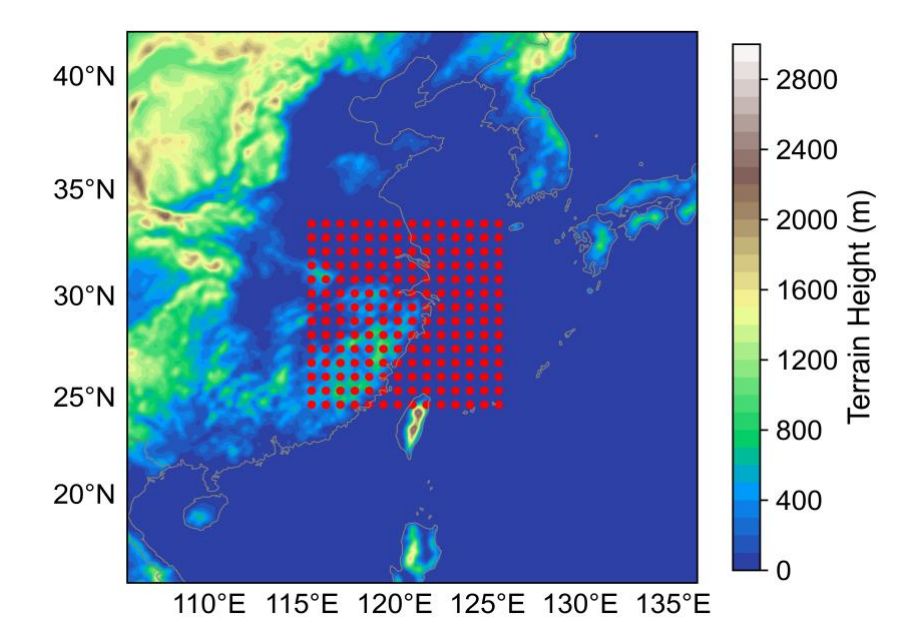


Figure 4: Model domain settings and locations of the selected points (red points) for single-point data assimilation experiments.

## 230 2.2.3 The EnSRF method

The synthetic observations were assimilated by the ENSRF algorithm. Within the GSI system, the scalable EnSRF framework proposed by Whitaker and Hamill (2002) is adopted. In the EnSRF framework, the ensemble mean and perturbations (the deviation from the mean) need to be updated separately (Kong et al., 2020, 2024). This section focuses specifically on the updating of the analysis variables.





Table 1: Configurations of WRF physical parameterization schemes for initializing ensemble members. The "combine" codes denote the microphysical, cumulus, and planetary boundary layer scheme in sequence. The superscripts (1)–(7) in the "combine" codes denote the spin-up times of 26h, 38h, 50h, 62h, 74h, 86h, and 98h, respectively.

microphysical schemes			cumulus schemes			PBL schemes	
scheme	number		scheme		number	scheme	number
Lin WSM5 WSM6 Goddard Thompson Morrison	1 2 3 4 5 6		Kain-Fritsch Betts-Miller-Janjic Grell-Devenyi Grell Old Kain-Fritsch		1 2 3 4 5	YSU MRF	1 2
member	combine	member	combine	member	combine	member	combine
01	1,1,1(1)	11	2,4,1 <sup>(4)</sup>	21	3,2,2 <sup>(7)</sup>	31	5,3,1 <sup>(3)</sup>
02	1,2,1(2)	12	2,5,1 <sup>(5)</sup>	22	4,1,1(1)	32	5,4,1 <sup>(4)</sup>
03	1,3,1 <sup>(3)</sup>	13	2,1,2 <sup>(6)</sup>	23	4,2,1(2)	33	5,5,1 <sup>(5)</sup>
04	1,4,1 <sup>(4)</sup>	14	2,2,2 <sup>(7)</sup>	24	4,3,1 <sup>(3)</sup>	34	5,1,2 <sup>(6)</sup>
05	1,5,1 <sup>(5)</sup>	15	3,1,1(1)	25	4,4,1 <sup>(4)</sup>	35	5,2,2 <sup>(7)</sup>
06	1,1,26	16	3,2,1 <sup>(2)</sup>	26	4,5,1 <sup>(5)</sup>	36	6,1,1(1)
07	1,2,2 <sup>(7)</sup>	17	3,3,1 <sup>(3)</sup>	27	4,1,2 <sup>(6)</sup>	37	6,2,1 <sup>(2)</sup>
08	2,1,1(1)	18	3,4,1 <sup>(4)</sup>	28	4,2,2 <sup>(7)</sup>	38	6,3,1 <sup>(3)</sup>
09	2,2,1 <sup>(2)</sup>	19	3,5,1 <sup>(5)</sup>	29	5,1,1(1)	39	6,4,1 <sup>(4)</sup>
10	2,3,1 <sup>(3)</sup>	20	3,1,26	30	5,2,1 <sup>(2)</sup>	40	6,5,1 <sup>(5)</sup>





The model state variables were updated following Eqs. (7) and (8), which update the ensemble mean and perturbations, 240 respectively:

$$\overline{X}^{a} = \overline{X}^{b} + K_{x} \left( y^{o} - H \overline{X}^{b} \right), \tag{7}$$

$$X_m^{a'} = X_m^{b'} - \widetilde{K_x} H X_m^{b'} , \qquad (8)$$

where  $\overline{X}^a$ ,  $\overline{X}^b$  represent the posterior and prior fields of the ensemble mean state variable, respectively. H is the observation operator that transforms the model state variables into the observation space.  $y^o$  is the observation. The m represents the m-th ensemble member, and  $X_m^{a'}$ ,  $X_m^{b'}$  represent the posterior and prior perturbation fields of the state variable for the m-th member.  $K_x$  and  $\widetilde{K_x}$  is Kalman gains, calculated by Eqs. (9) and (10).

$$K_{x} = \left[\alpha P^{b} H^{T}\right] (H P^{b} H^{T} + R)^{-1}, \tag{9}$$

$$\widetilde{K_x} = \left[1 + \sqrt{R/(HP^bH^T + R)}\right]^{-1} K_x \quad , \tag{10}$$

Where the  $P^b$  represents the background error covariance matrix and R represents the observation error covariance matrix.  $\alpha$  is distance-dependent localization function following Gaspari and Cohn (1999), which is applied via Schur multiplication to the  $P^b$  in order to restrict the influence of observations to a spatially limited region, thereby mitigating spurious correlations caused by finite ensemble size.

Finally, the analyses of the ensemble members can be expressed as:

$$X_m^a = \overline{X}^a + X_m^{a'} \,, \tag{11}$$

#### 250 2.3 Set-ups for single-observation and cycled experiments

Conducting a single-observation observation DA experiment before VIS reflectance DA within the OSSE framework is critically significant. The experiment assimilates a single-observation at target grid points to analyze changes in meteorological fields. The key advantages include: isolated impact assessment (changes exclusively induced by assimilated observations) and computational efficiency (single-grid calculation enabling rapid validation of DA workflows). This approach provides a foundation for evaluating VIS reflectance DA effectiveness. Two sets of single-observation experiments were conducted at 00:00 UTC and 02:00 UTC on September 21, 2024, with 196 observation points distributed as red dots in Fig. 4. We implemented a systematic sampling strategy, selecting every fifth grid point, and applied a 15 km localization radius. Given the model's 15 km horizontal resolution, the 75 km sampling interval significantly exceeds the localization radius. This ensured mutually independent DA processes that constitute an equivalent series of single-observation experiments. The observation



265

270



error was set to 0.1, which is close to the standard deviation of observation-minus-background statistics as is suggested by Zhou et al. (2025).

For the cycled experiment design, a single set of cycled DA experiments sufficed to meet the study's objective: validating the impact of assimilating AHI Channel 3 VIS reflectance on cloud fields and precipitation using the GSI-EnKF-CRTM-Vis DA technique. VIS reflectance is only available during daytime, so the operational window depends on solar zenith angle. For the East Asia simulation domain in September, sunrise and sunset occur approximately at 00:00 UTC and 08:00 UTC, respectively. We therefore initially set the DA window to 00:00 UTC–08:00 UTC.

However, the solar zenith angle at 02:00 UTC is obviously lower than that at 00:00 UTC. Sect. 3.2 demonstrated that a smaller solar zenith angle enhances the sensitivity of reflectance to CWP variations. This implies that discrepancies between model forecasted and actual cloud fields manifest as larger differences in satellite reflectance. Consequently, CWP errors generate stronger innovation vectors. This enables the DA to compute larger CWP analysis increments, thereby improving VIS reflectance DA efficacy. Simultaneously, at 00:00 UTC and 01:00 UTC, low solar zenith angles result in weak reflectance signals with high noise levels. Assimilating such data may introduce significant errors. We therefore started the cycled experiments at 02:00 UTC and concluded them at 08:00 UTC, using 1 hour interval. Following the DA window, the forecast extended until the next available VIS reflectance time the following day at 02:00 UTC.

We thinned the simulated observations to a 30 km resolution and applied a localization radius of 40 km as is suggested by Kugler et al. (2023). This ensured that the influence of each observation extended to neighbouring observation points, maintaining continuity in the analysis field. The control variables and observation error settings matched those used in the single-observation experiments.

#### 2.4 Evaluation Metrics

This study employed the Mean Bias (MB), Mean Absolute Error (MAE), Root Mean Square Error (RMSE), Equitable Threat Score (ETS) and False Alarm Rate (FAR) as metrics to quantitatively evaluate the effectiveness of VIS reflectance DA. The MB, MAE, RMSE are defined as:

$$MB = \frac{1}{N} \sum_{i=1}^{N} (f_i - o_i) , \qquad (12)$$

$$MAE = \frac{1}{N} \sum_{i=1}^{N} |f_i - o_i|,$$
 (13)

$$RMSE = \sqrt{\frac{1}{N} \sum_{i=1}^{N} (f_i - o_i)^2},$$
(14)

Where  $f_i$  and  $o_i$  are the forecasted and observed values at the *i*-th grid point, respectively, and N is the total number of evaluated grid points. MB quantifies the systematic deviation between forecasts and observations. MAE measures the average





285 magnitude of absolute errors without considering directionality. RMSE also measures average error magnitude. However, squaring the errors makes RMSE more sensitive to large deviations.

ETS is calculated as follows (Winterrath and Rosenow, 2007):

$$ETS = \frac{A - X}{A + B + C - X},\tag{15}$$

$$X = \frac{(A+B)(A+C)}{A+B+C+D} \,, \tag{16}$$

FAR is calculated by (Schaefer, 1990; Roebber, 2009):

$$FAR = \frac{B}{A+B} \,, \tag{17}$$

where A denotes the number of pixels where both forecast and observation exceed the threshold (hits); B denotes the number of pixels where forecast exceeds threshold but observation does not (false alarms). C denotes the number of pixels where observation exceeds threshold but forecast does not (misses). D denotes the number of pixels where neither forecast nor observation exceeds threshold (correct negatives).

## 3 Results

305

## 3.1 Single-observation experiments

Figure 5 details the relationship between the deviation of the observed reflectance from the ensemble mean (denoted as  $\delta_{REF}$ ) and the resulting CWP increment (denoted as  $\delta_{CWP}$ ) induced by the DA for a series of selected points. This scatter plot revealed a significant nonlinear positive correlation. It can be clearly observed from the figure that the overwhelming majority of data points are predominantly clustered within the first and third quadrants. This distribution shows that when observed reflectance exceeds the first-guess simulation ( $\delta_{REF} > 0$ ), it typically indicates greater actual cloud cover or thickness.

Consequently, the actual CWP is larger. At these points, the DA adjusted the cloud field state towards the observation. This adjustment manifests as an increase in CWP ( $\delta_{CWP} > 0$ ). Therefore, the trend in Fig. 5 shows that larger absolute differences between observed and background reflectance ( $|\delta_{REF}|$ ) correspond to larger absolute CWP adjustments ( $|\delta_{CWP}|$ ). This adjustment process aligns with the expectations of cloud microphysical processes.

Comparing single-observation experiments at 00:00 UTC and 02:00 UTC (Fig. 5a and 5b, respectively) revealed a clear difference. The absolute CWP increments ( $|\delta_{CWP}|$ ) generated by DA at 00:00 UTC (Fig. 5a) are significantly smaller overall than those generated at 02:00 UTC (Fig. 5b). This observational finding holds an important scientific significance as it offers strong, intuitive empirical support for the key conclusion discussed in Sect. 2.1 regarding experimental setup and observational sensitivity. Sect. 2.1 indicated that the solar zenith angle is a critical factor influencing the effectiveness of VIS reflectance DA. Specifically, it stated that smaller solar zenith angles yield greater and more effective CWP adjustments. The marked



320

325

330



difference between Fig. 5a and 5b not only quantitatively validate this physical mechanism but also clarify the optimal time window for implementing VIS reflectance DA.

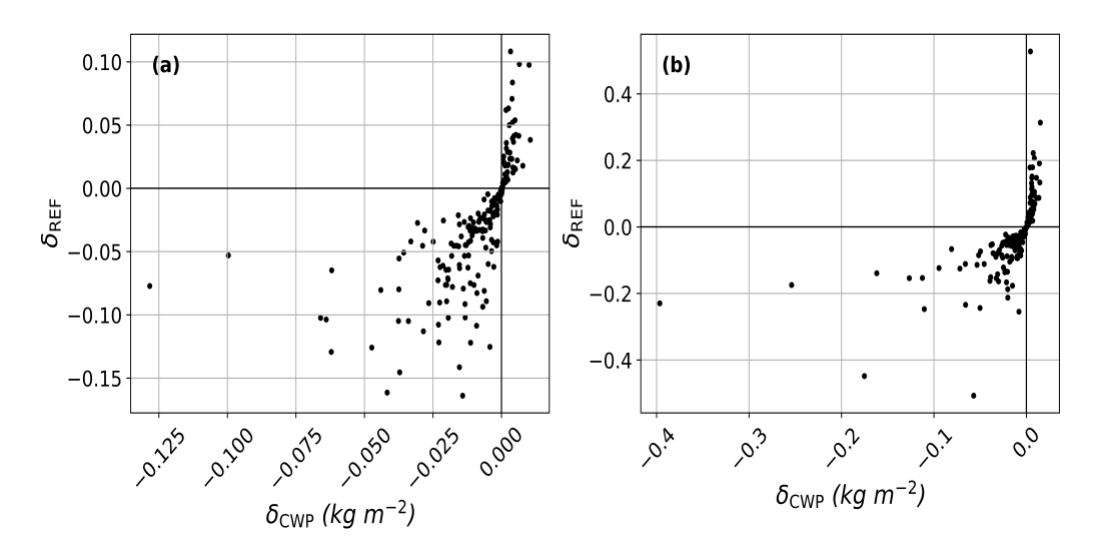


Figure 5: Scatter plots of the difference between observed and the ensemble mean simulated reflectance of the first guess ( $\delta_{REF}$ ) versus ensemble mean CWP analysis increment ( $\delta_{CWP}$ ) induced by single point visible reflectance assimilation. (a) 00:00 UTC; (b) 02:00 UTC.

Figure 6 shows the impact of VIS reflectance DA on the vertical structure of analysis variables at a random point selected from the 02:00 UTC experiment (Fig. 5b). The variables include temperature (T), water vapor mixing ratio (Q), liquid water mixing ratio (Ql, the sum of the mixing ratio of cloud and rain), and ice water mixing ratio (Qi, the sum of the mixing ratio of ice and snow). The results indicated that the influence of VIS reflectance DA on non-cloud variables (T, Q) is limited. The vertical profiles of T remain largely unchanged after DA, while the Q shows only a slight adjustment near 500 hPa. The specific improvement area is shown in fig. 6b. In contrast, cloud variables (Ql, Qi) exhibited distinct vertical structural adjustments. The primary adjustment for Ql occurred between the 500 hPa and 1000 hPa levels and the main adjustment for Qi was concentrated between 100 hPa and 600 hPa. The key factor responsible for the difference in vertical structural adjustments of the cloud variables lies in the magnitude of the background error covariance  $P^b$ . According to Eq. (9), the Kalman gain K is proportional to the  $P^b$ . Consequently, a larger  $P^b$  results in a larger K, leading to a larger analysis increment.

Overall, VIS reflectance DA has a limited effect on non-cloud variables. However, its correction effect on cloud variables is significant. This fundamental difference stems from the inherent difference in the sensitivity of the observation operator to different state variables. The sensitivity of VIS observations to cloud variables far exceeds that to non-cloud variables. The operator H is essentially the Jacobian matrix, whose elements consist of the partial derivatives of the state variables to the observations (Rochon et al., 2007). The partial derivatives of non-cloud variables to VIS observations are nearly zero. Therefore, the submatrix  $H_n$  for non-cloud variables approximates zero ( $H_n \approx 0$ ). This results in a very weak calculated Kalman





gain for non-cloud variables. Consequently, VIS observations cannot directly constrain them effectively. Conversely, the Kalman gain for cloud variables is significant, allowing effective constraint by the VIS reflectance.

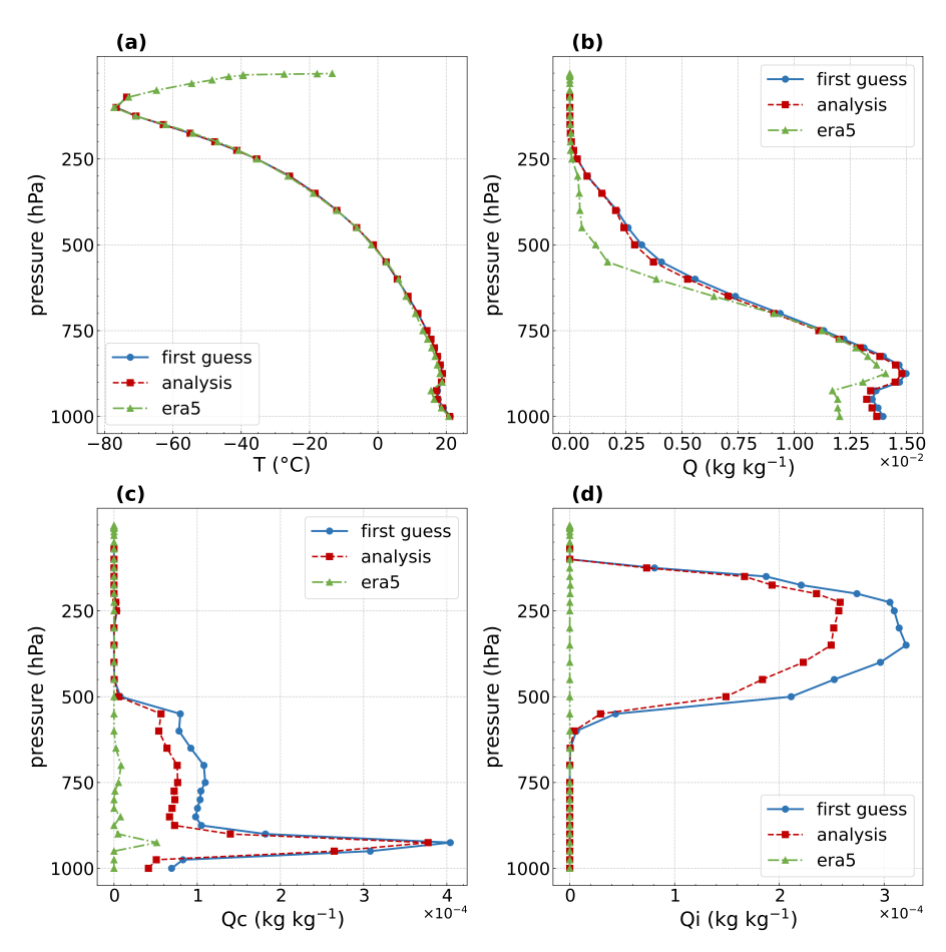


Figure 6: Vertical profiles of (a) temperature (T), (b) water vapor mixing ratio (Q), (c) liquid water mixing ratio (Ql = Qcloud + Qrain), and (d) ice water liquid water mixing ratio ( $Q_i$  = Qice + Qsnow) for: the nature run, the first guess and the analysis.

## 3.2 Cycled DA experiment

## **340 3.2.1 Impact on CWP**

345

To systematically evaluate the persistent correction capability of high-frequency VIS reflectance DA on cloud fields, this study conducted hourly cycled DA experiments from 02:00 to 08:00 UTC. Figure 7 compared the spatial distributions of CWP at 02:00, 04:00, 06:00, and 08:00 UTC. It includes the nature run, the ensemble means of the first guess, and the analysis increments. The increment fields are predominantly negative (Fig. 7a3–d3). This result indicated that VIS reflectance DA systematically corrected the prevalent overestimation of cloud water in the first guess.



355



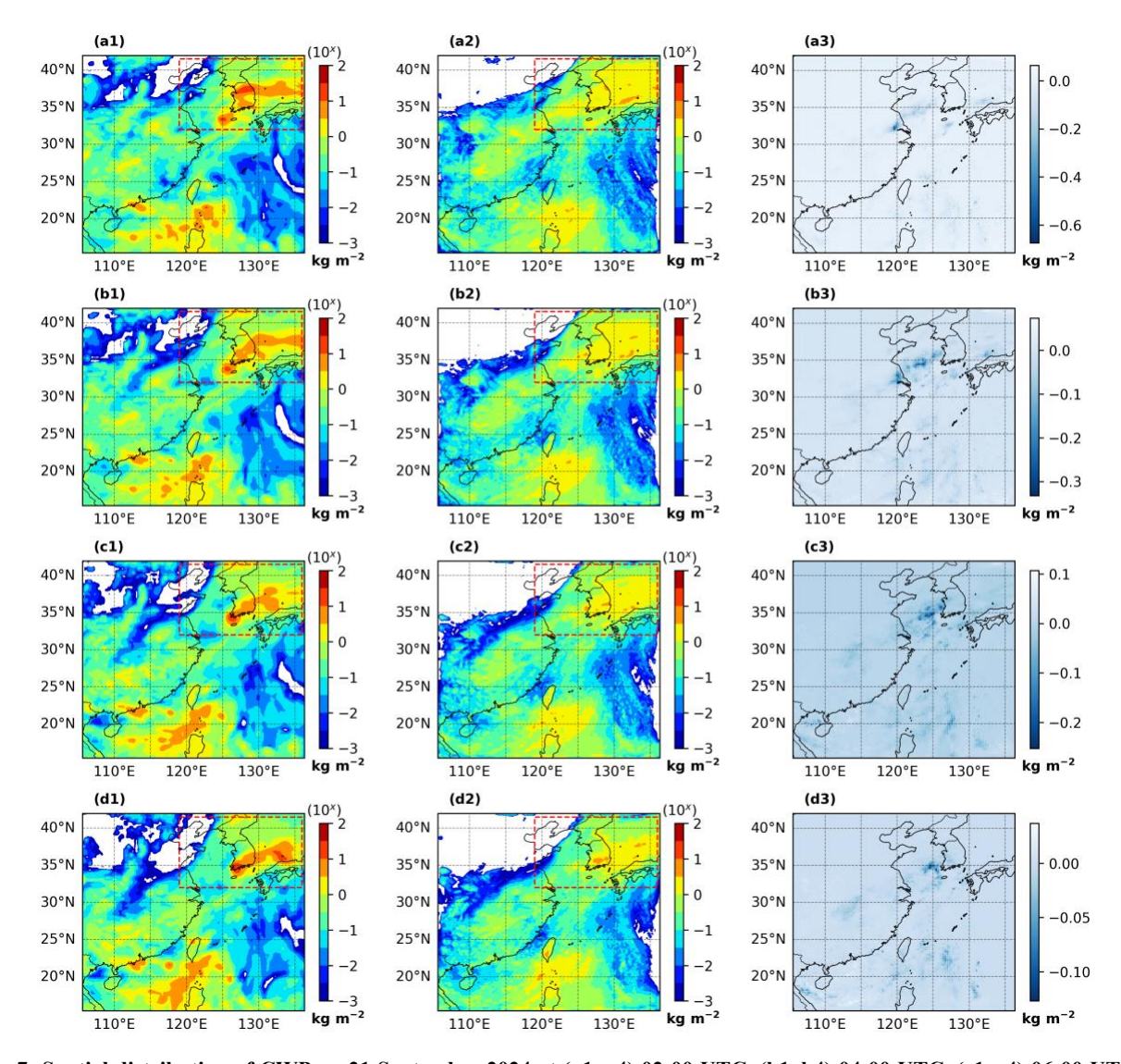


Figure 7: Spatial distribution of CWP on 21 September 2024 at (a1-a4) 02:00 UTC, (b1-b4) 04:00 UTC, (c1-c4) 06:00 UTC, and (d1-d4) 08:00 UTC, respectively. From left to right, the columns denote the nature run, the ensemble mean of the first guess, and the analysis increment (the analysis minus the ensemble mean of the first guess), respectively.

Spatially explicit CWP improvements are particularly observed in the domain east of 120° E and north of 35° N (demarcated by red rectangles). Within this sector, the first guess fields exhibit extensive overestimated cloud coverage (shown in yellow). As the cycled DA progresses, these overestimated cloud areas showed notable contraction. They gradually approached the distribution of the nature run. The correlation coefficient of CWP in this area between the first guess and the nature run increased from 0.45 to 0.6. Although the nature run exhibited localized extremely high values compared to the first



365

370

375



guess, the sensitivity of VIS reflectance to CWP gradually saturates when CWP > 10 kg·m<sup>-2</sup> as Fig. 1 shows. Under such conditions, the DA struggles to effectively correct cloud variables. This partially explains the absence of significant positive increments in the CWP fields. Concurrently, the maximum absolute CWP increment decreased progressively ( $|\Delta \text{CWP}_{\text{max}}|$  declines from 0.67 kg·m<sup>-2</sup> at 02:00 UTC to 0.13 kg·m<sup>-2</sup> at 08:00 UTC). This trend aligns with the decreasing background error covariance mechanism in cycled DA. Continuous DA absorbs observations and corrects background errors in the first guess. This reduces the Kalman gain in subsequent cycles that ultimately constrains the increment magnitude.

Therefore, continuous DA of VIS reflectance effectively suppressed cloud water overestimation in the first guess and achieved persistent optimization of cloud fields. Although the improvement magnitude weakened over successive cycles, the cumulative optimization effect increased progressively.

The ENSRF algorithm generates analysis increments based on the spread among the first guess ensemble members. Spatially, the standard deviation (STD) directly indicates this spread. Specifically, regions with larger STD values show higher ensemble dispersion, where significant increments are more likely to occur. This link exists because STD inherently characterizes background error. Larger STD values typically mean larger background errors, allowing larger increments (Sect. 3.1 provides the theoretical basis for this relationship). Figure 8a1–a4 display the spatial distributions of the first guess's CWP STD at 02:00, 04:00, 06:00, and 08:00 UTC. Comparing these with the increment distributions in Fig. 7a3–d3 revealed broad spatial consistency. High increment zones generally align with CWP STD maxima.

However, nonlinear model physics introduces simulation errors. These errors appear as mismatched spatial patterns between reflectance STD (Fig. 8b1–b4) and CWP STD distributions. Coupled with limitations in ensemble size, these factors disrupt the strict correspondence between increments and CWP STD distributions. Consequently, an anomaly occurs: significant increments sometimes do not appear in areas with high STD values.

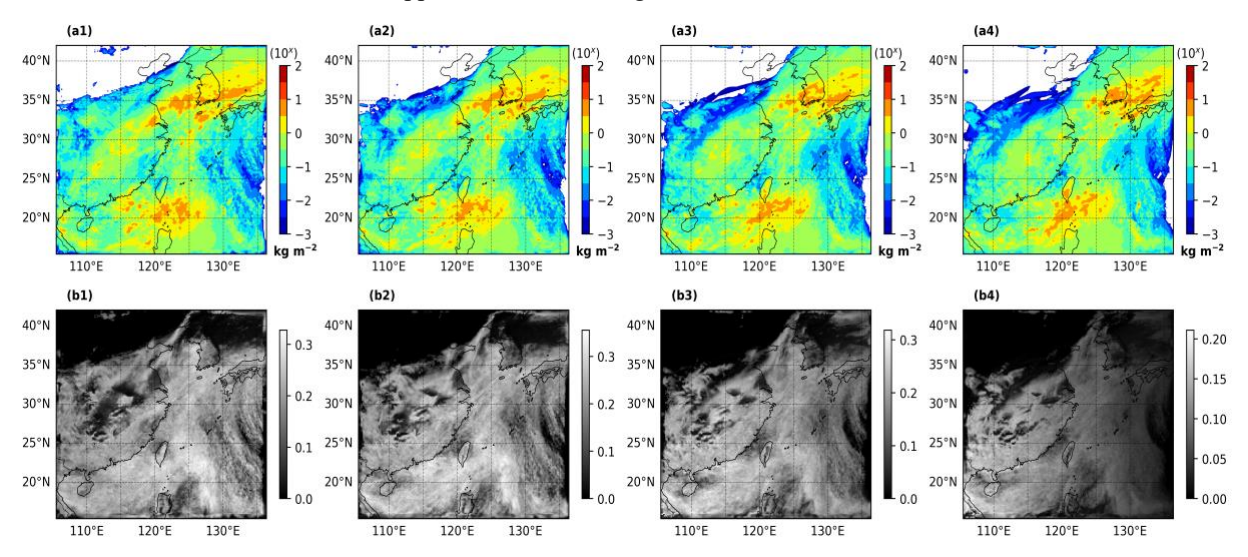


Figure 8: Standard deviation (STD) of of ensemble member CWP (a1-a4) and simulated reflectance (b1-b4). Columns from left to right correspond to 02:00, 04:00, 06:00, and 08:00 UTC.



385

390



Probability Density Function (PDF) analysis offers a unique statistical perspective for evaluating the performance of DA systems. Unlike traditional point-to-point error metrics, PDF comprehensively reveals changes in model variables. Based on this, we analyzed the PDFs of reflectance and CWP at DA times (02:00, 04:00, 06:00, and 08:00 UTC) using Fig. 9, comparing the nature run, the control run, the first guess, and the analysis. This analysis evaluated how assimilating VIS reflectance corrects the mean state and overall distribution of cloud variables. The results showed VIS reflectance DA has a significant downward adjustment effect on thin clouds (reflectance 0–0.2), while the correction effect on thick cloud areas remains relatively limited. The analysis fields' mean reflectance moved closer to the nature run's mean. Furthermore, both the distribution curves and the mean values demonstrated that the analysis field outperformed the first guess and the first guess outperformed the CTRL, which is consistent with expectations. The CWP PDF analysis most clearly shows DA correcting low CWP values (less than 10<sup>-1</sup> kg·m<sup>-2</sup>). This result further confirmed the effectiveness of the thin cloud correction identified in the reflectance analysis.

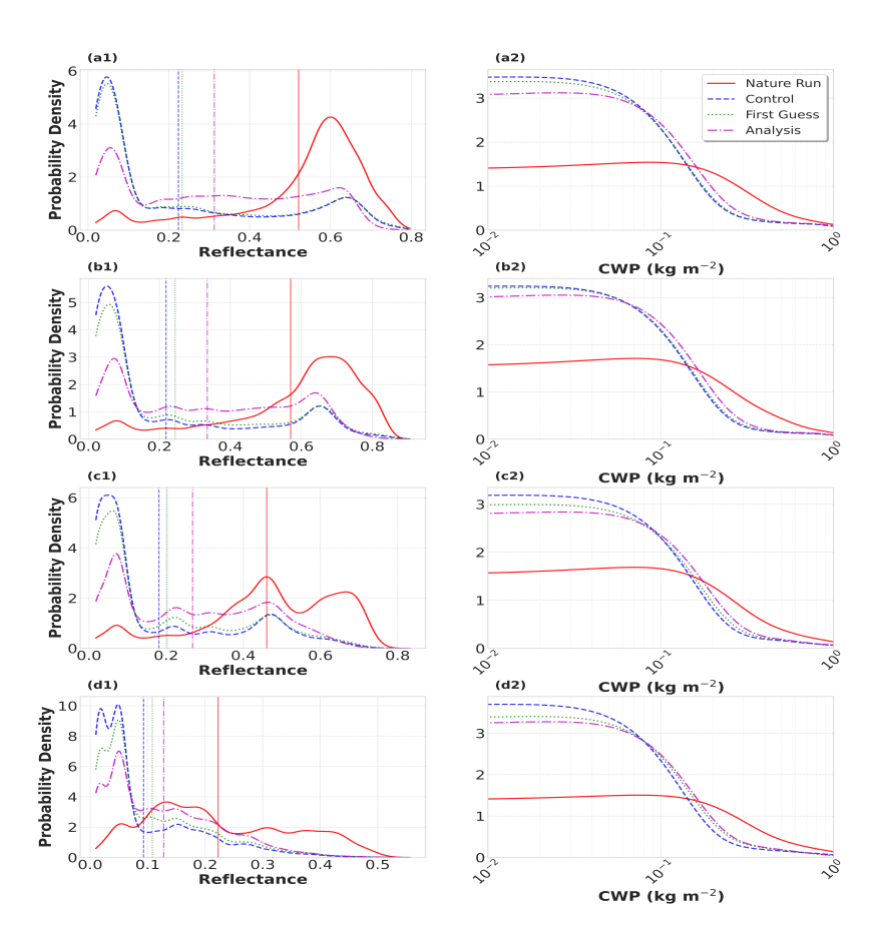


Figure 9: Probability density functions of reflectance (a1-d1) and CWP (a2-d2) at (a) 02:00, (b) 04:00, (c) 06:00, and (d) 08:00 UTC. Distributions are shown for nature run (red), the control run (blue), the first guess (green), and the analysis (magenta). The vertical lines indicate the mean values for each distribution.



400

405

410



As a supplement to spatial analysis, Figs. 10 and 11 revealed the temporal evolution of CWP MAE based on ensemble member 1. Results demonstrated that during the DA window (02:00 UTC–08:00 UTC, Fig. 10), the experimental group (EXP, labelled as EXP.) consistently exhibited lower MAE than the control group (CTRL, labelled as CTRL). EXP achieved a maximum instantaneous error reduction of 2.3 % at 03:00 UTC and a mean MAE reduction of 1.5 %. These results confirmed the persistent error suppression capability of VIS reflectance DA.

Throughout the experimental period encompassing forecast stages (02:00 UTC on September 21–02:00 UTC on September 21–02:00 UTC on September 22, Fig. 11), DA benefits for CWP errors persist for six subsequent hours. The peak MAE reduction (3.6 %) occurred at 13:00 UTC on 21 September. However, DA gained progressively diminishes as the forecast length increases. This decay stems from the diminishing background error covariance. Ultimately, the DA failed to counteract accumulating model errors. Although the assimilated initial field is closer to the nature run, its imbalance with the model's physical parameterizations leads to accelerated error growth during the early forecast stage. This inconsistency involves cloud microphysics parameterization and radiative transfer processes. Accelerated error growth began when DA gained vanish without new observational constraints. In contrast, the initial field of CTRL deviated from observations but was in a state of balance with the model's parameterizations. This balance helps mitigate long-term error accumulation to some extent. Consequently, EXP's MAE eventually surpassed CTRL's during later forecast stages.

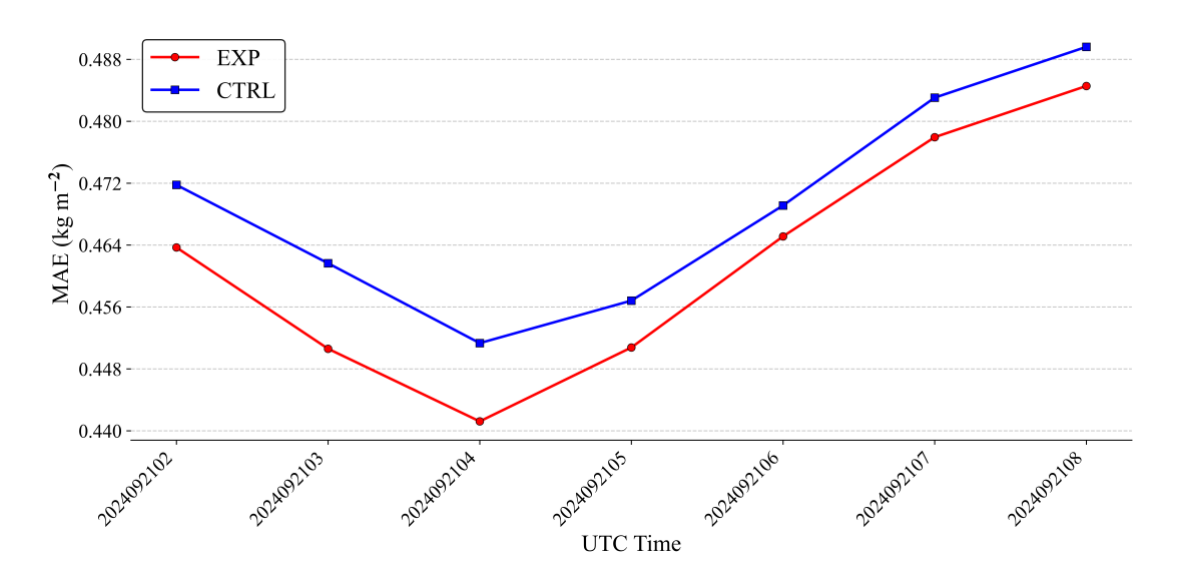


Figure 10: Temporal evolution of MAE of CWP during the assimilation window. EXP denotes the data assimilation experiment, while CTRL represents the control experiment.





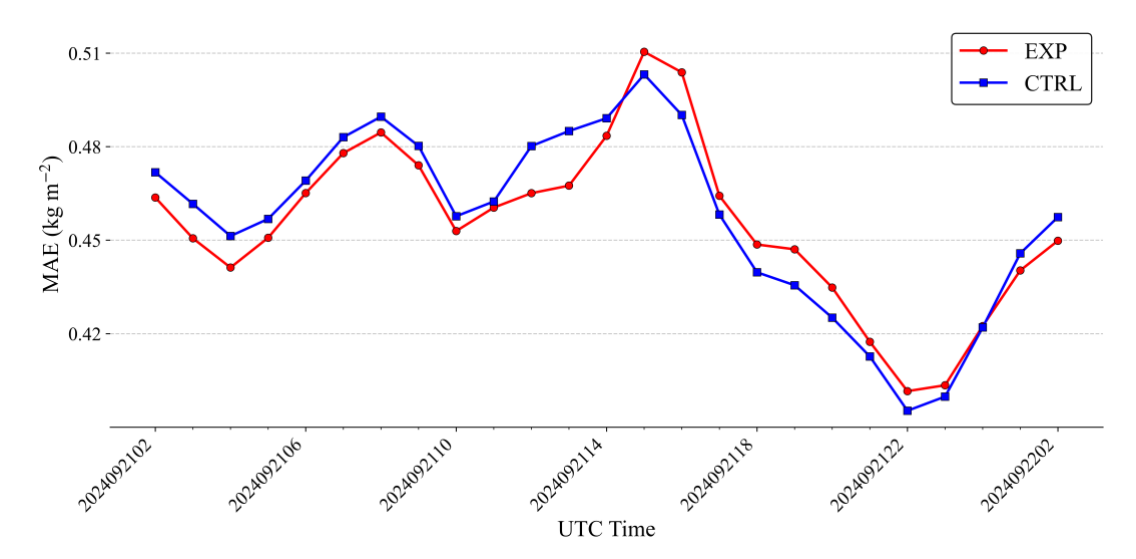


Figure 11. Temporal evolution of CWP MAE throughout the experimental period (assimilation + forecast periods). EXP denotes the data assimilation experiment, while CTRL represents the control run without assimilation.

## 3.2.2 Impact on non-cloud variables

Figure 12 shows the impact of VIS reflectance DA on non-cloud variables (U, V, T, Q), displaying vertical profiles of MB at 02:00, 04:00, 06:00, and 08:00 UTC. The results revealed nearly identical vertical profiles for the analysis and the first guess across all variables. This indicated that assimilating VIS reflectance has a negligible impact on non-cloud variables. The finding agrees with the single observation experiments.

Compared to CTRL, the analysis and first guess MB profiles aligned with CTRL at the initial DA stage (02:00 UTC). However, as the cycled DA progresses, the MB profiles for the analysis and first guess diverged from CTRL. While some regions or times exhibited improvements (e.g., U-component wind at 08:00 UTC from 800 to 1000 hPa (Fig. 12a4), V-component wind at 08:00 UTC from 500 to 700 hPa (Fig. 12b4), and T at 02:00 UTC from 700 to 800 hPa (Fig. 12c1)), deteriorations that values worse than CTRL also occurred (e.g., Fig. 12a3). These deteriorations occurred because assimilating VIS reflectance directly corrects cloud fields but makes almost no direct adjustment to non-cloud variables (wind, temperature, humidity). Cloud fields improvements can indirectly improve humidity and temperature via cloud microphysical processes (condensation, evaporation, deposition, sublimation) and cloud-radiation interactions under specific conditions (Scheck et al., 2020). This OSSE used ERA5 reanalysis data as the nature run to avoid the twin problem. Significant differences in numerical models, DA methods, and physical parameterization schemes between ERA5 (Hersbach et al., 2020) and our experimental setup likely obscure these beneficial indirect effects. Consequently, EXP's errors in non-cloud variables accumulated during forecasts, eventually surpassing CTRL. Future studies should validate simulated non-cloud variables against real observations. This will better reveal how VIS reflectance DA actually affects these variables.

430

420





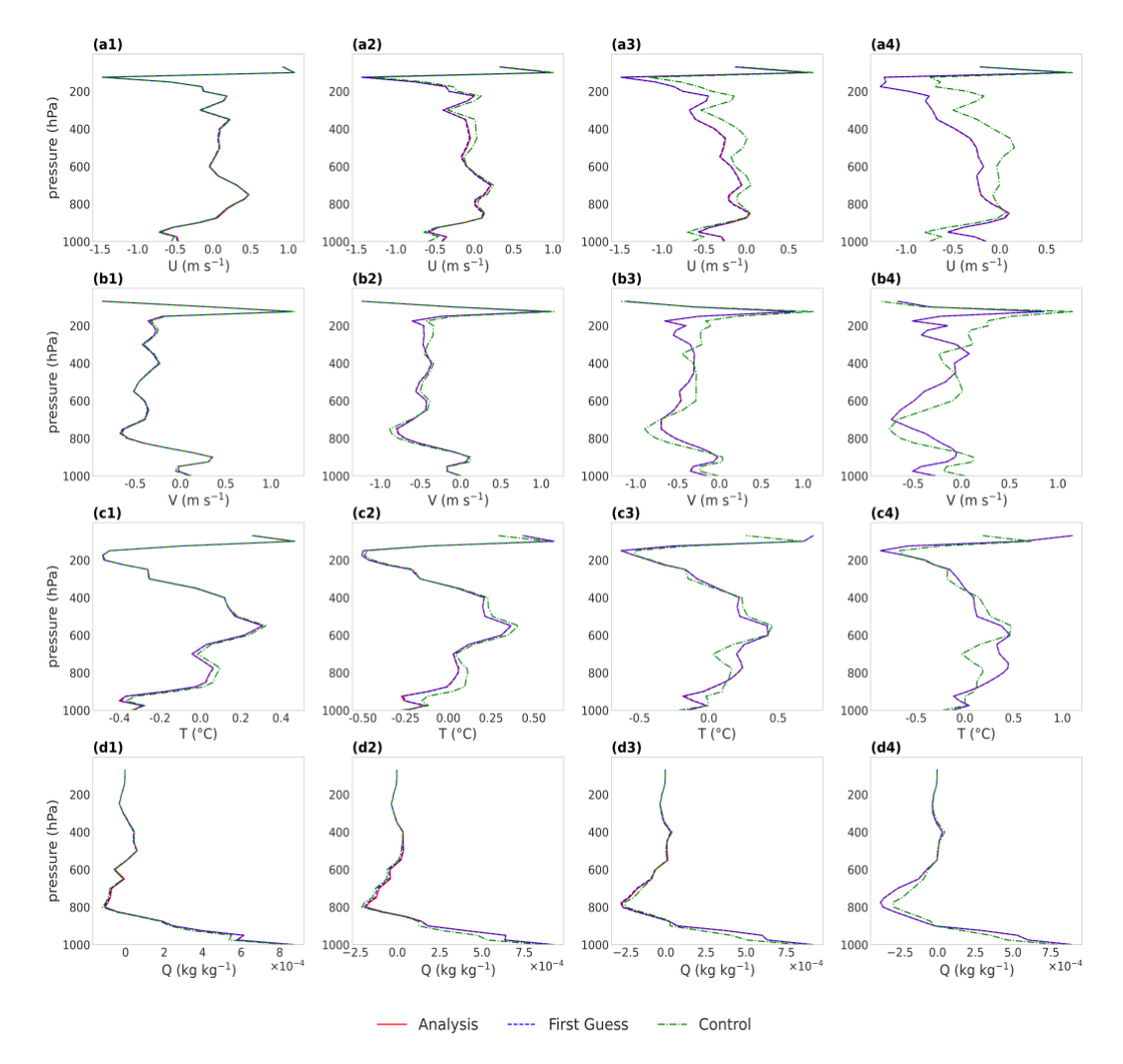


Figure 12: Vertical profiles of Mean Bias for non-cloud variables: (a) U-component wind, (b) V-component wind, (c) temperature (T), (d) water vapor mixing ratio (Q). Columns from left to right correspond to 02:00, 04:00, 06:00, and 08:00 UTC. Lines denote: the analysis (red), the first guess (blue), and the control run (green).

# 440 3.2.3 Impact on precipitation

445

Precipitation is a core element of meteorological forecasting, exhibiting formation processes linked closely to cloud genesis and development (Li et al., 2015). CWP quantifies the total hydrometeor content within clouds. It critically influences precipitation formation by governing droplet collision-coalescence efficiency and particle growth rates (Suzuki et al., 2010). Consequently, the adjustment of CWP through VIS reflectance DA will induces indirect effects on simulated precipitation.

This section evaluated the impact of assimilating VIS reflectance on model precipitation fields, focusing specifically on improvements in precipitation intensity and spatial distribution characteristics. Using ensemble member 1, we compared the results during both the DA window and the entire experimental period. Figure 13 compared the 7 hours accumulated



455

460



precipitation spatial distributions of the nature run, CTRL, and EXP during the DA window. Results revealed that while VIS reflectance DA did not substantially mitigate systematic precipitation overestimation surrounding the Korean Peninsula, it demonstrated significant corrective effects on false precipitation signals (accumulated precipitation is 10–30 mm) near Taiwan Island and China's southeastern coastal regions (shown in red rectangles). These corrections improved the spatial consistency of analysis with the nature run, indicating enhanced precipitation localization capability. Objective skill scores validated these improvements (ETS: higher better, Fig. 14a; FAR: lower better, Fig. 14b). Across thresholds (0.1, 2.5, 5, 10, 20, 40 mm), FAR decreased significantly at all levels, with the largest reduction of 28.7 % at 10 mm, confirming effective suppression of false precipitation warnings. ETS increased consistently across thresholds above 0.1 mm, demonstrating a definitive though modest improvement in the forecast skill for precipitation events.

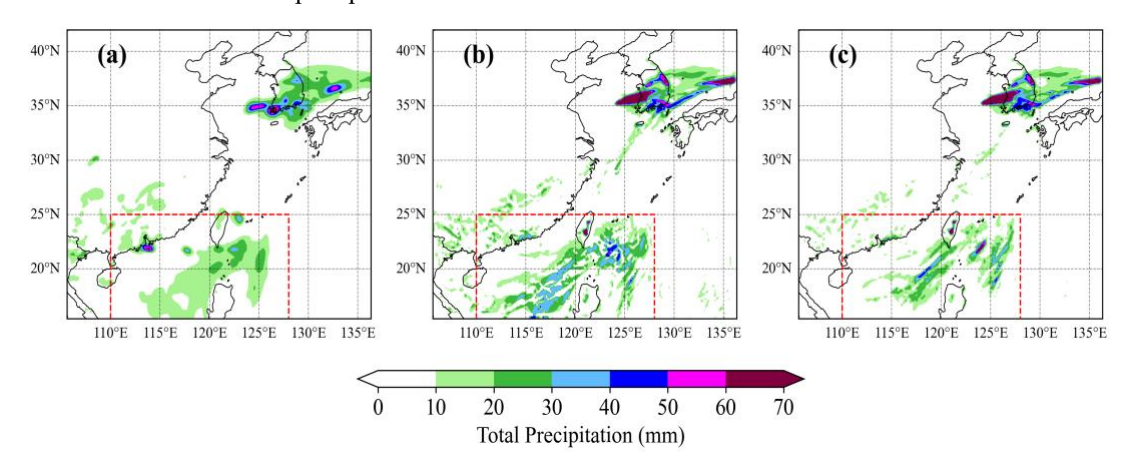


Figure 13: Spatial distribution of accumulated precipitation (mm) during the assimilation window (02:00–08:00 UTC, 7 hours total): (a) the nature run, (b) the control experiment, (c) the assimilation experiment.

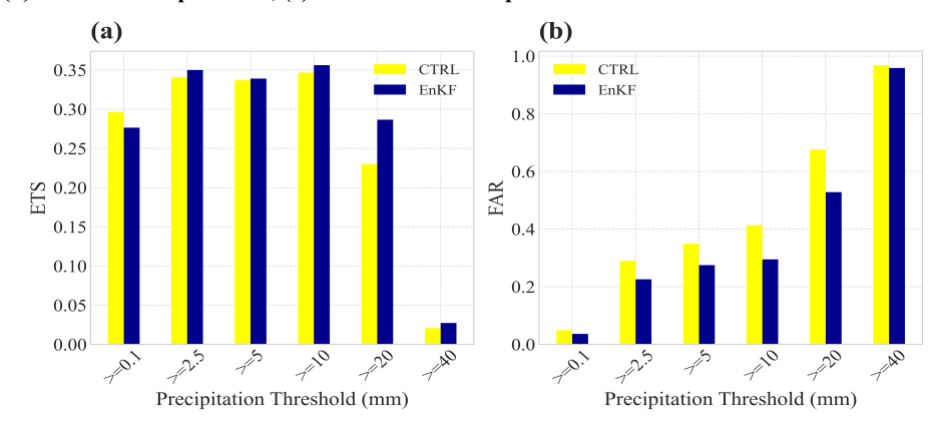


Figure 14: Forecast skill scores for varying precipitation (mm) thresholds during the assimilation window (02:00–08:00 UTC, 7 hours total): (a) ETS, (b) FAR. Results are shown for the control experiment (CTRL) and the assimilation experiment (EnKF).

To evaluate the improvement in the subsequent forecast precipitation field resulting from assimilating VIS reflectance, we analyzed the spatial distribution (Fig. 15) and skill scores (Fig. 16) over the entire 24 hours experiment period using the





same methodology as the above DA period analysis. Spatial analysis revealed significant improvements of the heavy rainfall area (120–150 mm) southwest of Taiwan Island and east of the Korean Peninsula (demarcated by red rectangles), aligning its extent more closely with the nature run. However, the overestimation of maximum precipitation intensity in the southwest of Taiwan Island was exacerbated, as forecast error growth exacerbated biases inherent in the model's physical parameterizations. This highlights a limitation of VIS reflectance DA in correcting the intense precipitation magnitude. The moderate-to-heavy precipitation region (30–60 mm) east of Taiwan shifted towards the nature run pattern, demonstrating the persistence of location corrections during DA. Skill score analysis (thresholds: 0.1/10/25/50/100/180 mm) shows: significant ETS improvement at 10, 50, and 100 mm thresholds but a clear reduction at 180 mm; FAR decreased by an average of 13.74 % below 180 mm, effectively reducing false alarms, though it increased slightly at 180 mm–consistent with the ETS reduction and corroborating heavy precipitation overestimation in the southwest of Taiwan Island.

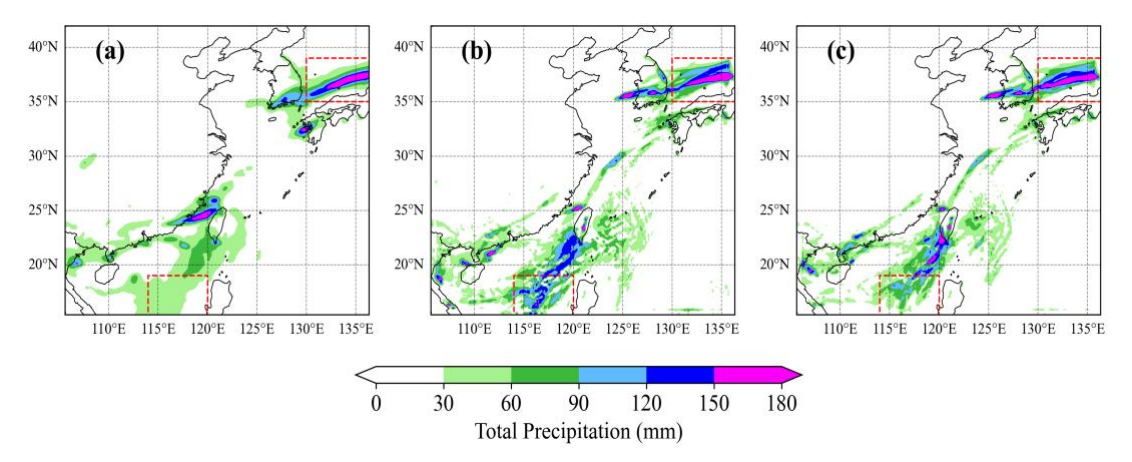


Figure 15: Spatial distribution of 24 hours accumulated precipitation (mm) throughout the experimental period: (a) the nature run, (b) the control experiment, (c) the assimilation experiment.

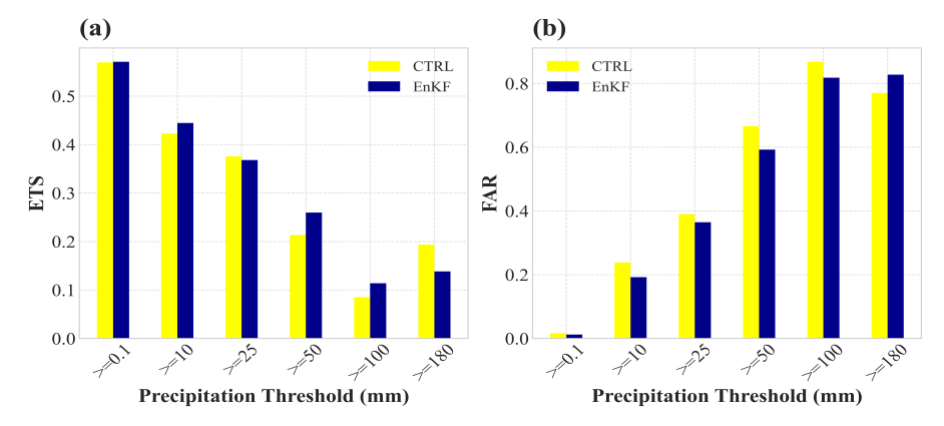


Figure 16: Forecast skill scores for varying precipitation thresholds (mm) throughout the 24 hours experimental period: (a) ETS, (b) FAR. Results are shown for the control experiment (CTRL) and the assimilation experiment (EnKF).





## 4 Conclusions

485

490

495

500

505

510

We developed the GSI-EnKF-CRTM-Vis DA technique for assimilating satellite VIS reflectance data. The performance of the newly developed technique is validated by assimilating the synthetic Himawari-8 AHI 0.64 µm reflectance data under an OSSE framework. We conducted two groups of experiments: single-observation and cycled DA experiments. Key configurations included: 40 ensemble members, an observation error of 0.1, 30km thinned observations, an hourly DA frequency and a 40km localization radius. The core findings are as follows:

The single-observation tests revealed the differential impact of VIS reflectance DA on cloud versus non-cloud variables and its capability to correct CWP. Results indicated an improvement in the vertical structure of the liquid water mixing radio (Ql) and the ice water mixing radio (Qi), while the influence on non-cloud variables (temperature, water vapor mixing ratio) was minimal. This improvement stems from the VIS observation operator  $\mathbf{H}$  being far more sensitive to cloud variables. Consequently, the Kalman gain is substantial for cloud variables but nearly zero for non-cloud variables. Since CWP is intrinsically the vertical integral of Ql and Qi, the effective adjustment of their vertical distributions consequently optimized the CWP estimation. Analysis confirmed that the innovation ( $\delta_{REF}$ , defined as the difference between the observed reflectance and the ensemble mean of the first guess) and the CWP increment ( $\delta_{CWP}$ ) exhibited consistent sign changes. We also observed an approximately proportional relationship between  $|\delta_{CWP}|$  and  $|\delta_{REF}|$ . This adjustment process is consistent with theoretical expectations and aligns with the findings of Zhou et al (2022).

The cycled DA experiment systematically investigated the impact of VIS reflectance DA on: the spatial correction of CWP, the probability distribution characteristics of reflectance and CWP, the temporal evolution of CWP error (as measured by MAE), the vertical structure of non-variables (U, V, T, Q) and precipitation forecasts. Regarding CWP correction, results showed that VIS reflectance DA primarily produced negative increments, i.e., mitigating the prevalent overestimation of cloud water content in the first guess. Larger absolute increments often occurred where background CWP standard deviation (STD) was high. Higher STD increases background error covariance, leading to larger Kalman gain and increments. For probability distributions, DA significantly corrected the PDFs for thin clouds (reflectance 0-0.2) and low CWP values (less than 0.1 kg·m<sup>-</sup> 2), shifting the analysis distribution closer to the nature run. In terms of CWP error assessment, DA significantly reduced the mean absolute error (MAE) of CWP by an average of 1.5 % during the DA period, demonstrating sustained error suppression. Notably, CWP MAE continued decreasing for up to 6 hours after DA stopped, reaching a maximum reduction of 3.6 % at fifth hour. Concerning non-cloud variables (U, V, T, Q), vertical profiles of MB confirmed negligible direct adjustment from VIS reflectance DA, due to the observation operator's near-zero sensitivity. Regarding precipitation forecast improvement, the DA notably enhanced the simulation of spurious weak precipitation in the DA window over Taiwan Island and the southeastern coastal regions of China. Quantitative verification (ETS, FAR) indicated improvements: ETS increased for all precipitation thresholds except 0.1 mm and FAR reduced across all thresholds. As the forecast time extends, although DA still improved precipitation spatial patterns, it exacerbated the extreme overestimation of heavy rainfall (180 mm threshold), manifested by reduced ETS and increased FAR at this threshold. Improvements in ETS and FAR persisted at other thresholds.



520

525

530

535



In summary, VIS reflectance DA efficiently corrects cloud variables. It significantly optimizes CWP spatial structure, suppresses systematic errors, and improves weak precipitation depiction. However, its effectiveness in improving extreme precipitation forecasts remains limited. Furthermore, it may degrade non-cloud variables in extended forecasts due to unconstrained error propagation. This highlights the need for further refinement of the technique for extreme weather events.

Code availability. WRF-ARW version 4.1.5 (Skamarock et al., 2008) was used in this study. The source code is available at https://github.com/wrf-model/WRF/releases/tag/v4.1.5 (last access: 30 October 2023). Version 2.1.3 of CRTM (Johnson et al., 2023) source code is publicly available at https://ftp.emc.ncep.noaa.gov/jcsda/CRTM/REL-2.1.3/crtm\_v2.1.3.tar.gz (last access: 26 June 2024). The source code for standard GSI v3.7\_EnKF v1.3 is publicly available at https://github.com/paocorrales/comGSIv3.7\_EnKFv1.3 (last access: 22 March 2024). The source codes of the CRTM v2.1.3 and the newly developed GSI-EnKF-CRTM-Vis data assimilation technique were uploaded at https://doi.org/10.5281/zenodo.17445798 (Luo et al., 2025).

*Data availability.* The ERA5 hourly data on pressure levels and on single levels were downloaded at https://doi.org/10.24381/cds.bd0915c6 (Hersbach et al., 2023a) and https://doi.org/10.24381/cds.adbb2d47 (Hersbach et al., 2023b). The NCEP GFS 0.25 Degree Global Forecast Grids data (National Centers for Environmental Prediction et al., 2015) are available at https://doi.org/10.5065/D65D8PWK. The processed data and the visualization scripts are available at https://doi.org/10.5281/zenodo.17445798 (Luo et al., 2025). All data are available upon request from Chong Luo.

Author contributions. ChoL devised the methodology, collected the experimental data including NCEP GFS and ERA5, downloaded and compiled the CRTM and GSI models, designed and conducted the experiments, and wrote the paper. YZ supported the development of the interface for assimilating Himawari-8 visible reflectance data and collaborated on the experiment design and result analysis. YL contributed to the selection of the experimental case through scientific discussion. WH contributed part of scripts for presenting results. BY provided the calculation formulas for the input parameters of CRTM. CL provided valuable insights for the model development. All authors were involved in discussions throughout the development and experimental phases, and all authors reviewed the paper.

Competing interests. The contact author has declared that none of the authors has any competing interests.

**Disclaimer.** Publisher's note: Copernicus Publications remain neutral with regard to jurisdictional claims in published maps and institutional affiliations.

545





Acknowledgements. We acknowledge the High Performance Computing Center of Nanjing University of Information Science & Technology for their support of this work. We are grateful to the anonymous reviewers for their constructive comments and suggestions.

550 Financial support. This study is supported by the National Natural Science Foundation of China (U2442215 and 42305161)

#### References

- Arnold, C. P., and Dey, C. H.: Observing-Systems Simulation Experiments: Past, Present, and Future, Bull. Amer. Meteor. Soc., 67, 687–695, doi:10.1175/1520-0477(1986)067<0687:OSSEPP>2.0.CO;2, 1986.
- Bauer, P., Geer, J. A., Lopez, P., and Salmond, D.: Direct 4D-Var assimilation of all-sky radiances. Part I: Implementation, Q. J. Roy. Meteor. Soc., 136, 1868–1885, doi:10.1002/qj.659, 2010.
  - Bauer P., Thorpe A., and Brunet G.: The quiet revolution of numerical weather prediction, Nature, 525, 47–55, doi:10.1038/nature14956, 2015.
  - Bonavita, M., Lean, P., and Holm, E.: Nonlinear effects in 4D-Var, Nonlin. Processes Geophys., 25, 713–729, doi: 10.5194/npg-25-713-2018, 2018.
- Chambon, P., and Geer A. J.: All-sky assimilation of Megha-Tropiques/SAPHIR radiances in the ECMWF numerical weather prediction system, European Centre for Medium Range Weather Forecasts, doi:10.21957/4h085eb9, 2017.
  - Chen, K., Suo, Z. H., Han, W., and Cai, B. W.: OSSEs on the FY-4M Geostationary Microwave Satellite Based on CMA-GFS and CMA-MESO, IEEE Trans. Geosci. Remote Sens., 62, 1–19, doi:10.1109/TGRS.2024.3487859, 2024.
  - Chen, K. Y., Chen, Z. X., Xian, Z. P., and Li, G. C.: Impacts of the All-Sky Assimilation of FY-3C and FY-3D MWHS-2 Radiances on Analyses and Forecasts of Typhoon Hagupit, Remote Sens., 15, 2279, doi:10.3390/rs15092279, 2023.
  - Errico, R. M., Bauer, P., and Mahfouf, J.: Issues Regarding the Assimilation of Cloud and Precipitation Data, J. Atmos. Sci., 64, 3785–3798, doi:10.1175/2006JAS2044.1, 2007.
  - Gaspari, G., and Cohn, S. E.: Construction of correlation functions in two and three dimensions. Q. J. Roy. Meteor. Soc., 125, 723–757, doi: 10.1002/qj.49712555417, 1999.
- Geer, A. J., Bauer, P., and Lopez, P.: Direct 4D-Var assimilation of all-sky radiances. Part II: assessment, Q. J. Roy. Meteor. Soc., 136, 1886–1905, doi:10.1002/qj.681, 2010.
  - Geer, A. J., Migliorini, S., and Matricardi, M.: All-sky assimilation of infrared radiances sensitive to mid- and upper-tropospheric moisture and cloud, Atmos. Meas. Tech., 12, 4903–4929, doi:10.5194/amt-12-4903-2019, 2019.
- Heinze, R., Dipankar, A., Henken, C. C., Moseley, C., Sourdeval, O., Trömel, S., Xie, X. X., Adamids, P., Ament, F., Baars,
  H., Barthlott, C., Behrendt, A., Blahak, U., Bley, S., Brdar, S., Brueck, M., Crewell, S., Deneke, H., Girolamo, P. D., Evaristo,
  R., Fischer, J., Frank, C., Friederichs, P., Göcke, T., Gorges, K., Hande, L., Hanke, M., Hansen, A., Hege, H. C., Hoose, C.,
  Jahns, T., Kalthoff, N., Klocke, D., Kneifel, S., Knippertz, P., Kuhn, A., Laar, T., V., Macke, A., Maurer, V., Mayer, B.,





- Meyer, C. I., Muppa, A. K., Neggers, R. A. J., Orlandi, E., Pantillon, F., Pospichal, B., Röber, N., Scheck, L., Seifert, A., Seifert, P., Senf, F., Siligam, P., Simmer, C., Steinke, S., Stevens, B., Wapler, K., Weniger, M., Wulfmeyer, V., Zängl, G.,
  Zhang, D., and Quaas, J.: Large-eddy simulations over Germany using ICON: A comprehensive evaluation, Q. J. Roy. Meteor. Soc., 143, 69–100, doi:10.1002/qj.2947, 2017.
  - Hersbach, H., Bell, B., Berrisford, P., Biavati, G., Horányi, A., Muñoz Sabater, J., Nicolas, J., Peubey, C., Radu, R., Rozum, I., Schepers, D., Simmons, A., Soci, C., Dee, D., and Thépaut, J.-N.: ERA5 hourly data on pressure levels from 1940 to present, Copernicus Climate Change Service (C3S) Climate Data Store (CDS) [data set], doi: 10.24381/cds.bd0915c6, 2023a.
  - Hersbach, H., Bell, B., Berrisford, P., Biavati, G., Horányi, A., Muñoz Sabater, J., Nicolas, J., Peubey, C., Radu, R., Rozum, I., Schepers, D., Simmons, A., Soci, C., Dee, D., and Thépaut, J.-N.: ERA5 hourly data on pressure levels from 1940 to present, Copernicus Climate Change Service (C3S) Climate Data Store (CDS), [data set], doi: 10.24381/cds.adbb2d47, 2023b.
- Hersbach, H., Bell, B., Berrisford, P., Hirahara, S., Horányi, A., Muñoz-Sabatr, J., Nicolas, J., Peubey, C., Radu, R., Schepers, D., Simmons, A., Soci, C., Abdalla, S., Abellan, X., Balsamo, G., Bechtold, P., Biavati, G., Bidlot, J., Bonavita, M., Chiara, G. D., Dahlgren, P., Dee, D., Diamantakis, M., Dragazi, R., Flemming, J., Forbes, R., Fuentes, M., Geer, A., Haimberger, L., Healy, S., Hogan, R. J., Hólm, E., Janisková, M., Keeley, S., Laloyaux, P., Lopez, P., Lupu, C., Radnoti, G., Rosnay, P., Rozum, I., Vamborg, F., Villaume, S., and Thépaut, J. N.: The ERA5 global reanalysis, Q. J. Roy. Meteor. Soc., 146, 1999–2049, doi:10.1002/qj.3803, 2020.
  - Honda, T., and Miyoshi, T., Lien, G. Y., Nishizawa, S., Yoshida, R., Adachi, S. A., Terasaki, K., Okamoto, K., Tomita, H., and Bessho, K.: Assimilating All-Sky Himawari-8 Satellite Infrared Radiances: A Case of Typhoon Soudelor (2015), Mon. Weather Rev., 146, 213–229, doi:10.1175/MWR-D-16-0357.1, 2018.
- Hong, S.Y., Dudhia, J., and Chen, S.H.: A revised approach to ice microphysical processes for the bulk parameterization of clouds and precipitation, Mon. Weather Rev., 132, 103–120, doi:10.1175/1520-0493(2004)132%3C0103:ARATIM%3E2.0.CO;2, 2004.
  - Houtekamer, P. L., and Zhang, F.: Review of the Ensemble Kalman Filter for Atmospheric Data Assimilation, Mon. Weather Rev., 144, 4489–4532, doi:10.1175/MWR-D-15-0440.1, 2016.
- Johnson, B. T., Dang, C., Stegmann, P., Liu, Q., Moradi, I., and Auligne, T.: The Community Radiative Transfer Model (CRTM): Community-Focused Collaborative Model Development Accelerating Research to Operations, Bull. Amer. Meteor. Soc., 104, E1817–E1830, doi:10.1175/BAMS-D-22-0015.1, 2023.
  - King, M. D., Platnick, S., Yang, P., Arnold, G. T., Gray, M. A., Riedi, J. C., Ackerman, S. A., and Liou, K.: Remote Sensing of Liquid Water and Ice Cloud Optical Thickness and Effective Radius in the Arctic: Application of Airborne Multispectral MAS Data, J. Atmos. Oceanic Technol., 21, 857–875, doi:10.1175/1520-0426(2004)021<0857:RSOLWA>2.0.CO;2, 2004.



615

630



- 610 Kong, R., Xue, M., Fierro, A. O., Jung, Y. S., Liu, C., Mansell, E. R., and MacGorman, D. R.: Assimilation of GOES-R Geostationary Lightning Mapper Flash Extent Density Data in GSI EnKF for the Analysis and Short-Term Forecast of a Mesoscale Convective System, Mon. Weather Rev., 148, 2111–2133, doi:10.1175/MWR-D-19-0192.1, 2020.
  - Kong, R., Xue, M., Mansell, E. R., Liu, C. S., and Fierro, A. O.: Assimilation of GOES-R Geostationary Lightning Mapper Flash Extent Density data in GSI 3DVar, EnKF, and Hybrid En3DVar for the analysis and short-term forecast of a supercell storm case, Adv. Atmos. Sci., 41, 263–277, doi:10.1007/s00376-023-2340-2, 2024.
  - Kugler, L., Anderson, J.L., and Weissmann, M.: Potential impact of all-sky assimilation of visible and infrared satellite observations compared with radar reflectivity for convective-scale numerical weather prediction, Q. J. Roy. Meteor. Soc., 149, 3623–3644, doi:10.1002/qj.4577, 2023.
- Lei, L. L., Wang, Z. R., and Tan, Z. M.: Integrated hybrid data assimilation for an ensemble Kalman filter, Mon. Weather Rev.,149,4091–4105, doi:10.1175/MWR-D-21-0002.1, 2021.
  - Li, Y. Y., K, X. W., Fang, L. X., and Sun, G. R.: Analysis and model evaluation of the relationship between clouds and precipitation over eastern China, Acta Meteorol. Sin, 4, 766–777, doi:10.11676/qxxb2015.042, 2015.
  - Lopez, P.: Cloud and Precipitation Parameterizations in Modeling and Variational Data Assimilation: A Review, J. Atmos. Sci., 64, 3766–3784, doi:10.1175/2006JAS2030.1, 2007.
- 625 Lou, S., Zhu, L., Qiu, X. X., Chen, G. Z., Yuan, S., and Zhou, S. N.: Impact of EnKF assimilating Himawari-8 all-sky infrared radiance on the forecasting of a warm-sector rainstorm event, Sci. China Earth Sci., 67, 3110–3127, doi:10.1007/s11430-023-1403-5, 2024.
  - Luo, C., Zhou, Y. B., Liu, Y. B., Han, W., Yao, B., and Liu, C.: GSI-EnKF-CRTM-Vis Data Assimilation Technique: Model Code, Processed Data and Visualization Scripts for GMD-2025-4553, Zenodo [data set], doi: 10.5281/zenodo.17445798, 2025.
  - Ma, S., Zhang, W. M., Cao, X. Q., Zhao, Y., L., and Liu, B. N.: Assimilation of all-sky radiance from the FY-3 MWHS-2 with the Yinhe 4D-Var system, J. Meteorol. Res., 36, 750–766, doi:10.1007/s13351-022-1208-1, 2022.
  - Migliorini, S., and Candy, B.: All-sky satellite data assimilation of microwave temperature sounding channels at the Met Office, Q. J. Roy. Meteor. Soc., 145, 867–883, doi:10.1002/qj.3470, 2019.
- Nakajima, T., and King, M. D.: Determination of the optical thickness and effective particle radius of clouds from reflected solar radiation measurements. Part I: Theory, J. Atmos. Sci., 47, 1878–1893, doi:10.1175/15200469(1990)047<1878:DOTOTA>2.0.CO;2, 1990.
  - National Centers for Environmental Prediction, National Weather Service, NOAA and U.S. Department of Commerce, updated daily: NCEP GFS 0.25 Degree Global Forecast Grids Historical Archive, Research Data Archive at the National Center for Atmospheric Research, Computational and Information Systems Laboratory [data set], doi:10.5065/D65D8PWK, 2015.
  - Okamoto, K.: Assimilation of overcast cloudy infraredradiances of the geostationary MTSAT-1R imager, Q. J. Roy. Meteor. Soc., 139, 715–730, doi:10.1002/qj.1994, 2012.





- Otkin, J. A.: Clear and cloudy sky infrared brightness temperature assimilation using an ensemble Kalman filter, J. Geophys. Res., 115, D19207, doi:10.1029/2009JD013759, 2010.
- Otkin, J. A.: Assimilation of water vapor sensitive infrared brightness temperature observations during a high impact weather event, J. Geophys. Res., 117, D19203, doi:10.1029/2012JD017568, 2012.
  - Platnick, S., King, M. D., Ackerman, S. A., Menzel, W. P., Baum, B. A., and Riedi, J. C.: The MODIS cloud products: algorithms and examples from Terra, IEEE Trans. Geosci. Remote Sens., 41, 459–473, doi:10.1109/TGRS.2002.808301, 2003.
- Polkinghorne, R., and Vukicevic, T.: Data Assimilation of Cloud-Affected Radiances in a Cloud-Resolving Model, Mon. Weather Rev., 139, 755–773, doi:10.1175/2010MWR3360.1, 2011.
  - Poterjoy, J.: A Localized Particle Filter for High-Dimensional Nonlinear Systems, Mon. Weather Rev., 144, 59–76, doi:10.1175/MWR-D-15-0163.1, 2016.
- Rochon, Y. J., Garand, L., Turner, D. S. and Polavarapu, S.: Jacobian mapping between vertical coordinate systems in data assimilation, Q. J. Roy. Meteor. Soc., 133, 1547–1558, doi:10.1002/qj.117, 2007.
  - Roebber, P. J.: Visualizing Multiple Measures of Forecast Quality, Wea. Forecasting, 24, 601–608, doi:10.1175/2008WAF2222159.1, 2009.
  - Schaefer, J. T.: The Critical Success Index as an Indicator of Warning Skill, Wea. Forecasting, 5, 570–575, doi:10.1175/1520-0434(1990)005<0570:TCSIAA>2.0.CO;2, 1990.
- 660 Scheck, L., Weissmann, M., and Bach, L.: Assimilating visible satellite images for convective-scale numerical weather prediction: A case-study, Q. J. Roy. Meteor. Soc., 146, 3165–3186. doi:10.1002/qj.3840, 2020.
  - Schröttle, J., Weissmann, M., Scheck, L., and Hutt, A.: Assimilating Visible and Infrared Radiances in Idealized Simulations of Deep Convection, Mon. Weather Rev., 148, 4357–4375, doi:10.1175/MWR-D-20-0002.1, 2020.
  - Skamarock, W. C., Klemp, J. B., Dudhia, J., Gill, D. O., Barker, D. M., Duda, M. G., Wang, X.-Y., Wang, W., and Power, J.
- 665 G.: A Description of the Advanced Research WRF Version 3 (No. NCAR/TN-475+STR), University Corporation for Atmospheric Research, doi:10.5065/D68S4MVH, 2008.
  - Stengel, M., Lindskog, M., Undén, P., and Gustafsson, N.: The impact of cloud-affected IR radiances on forecast accuracy of a limited-area NWP model, Q. J. Roy. Meteor. Soc., 139, 2081–2096, doi:10.1002/qj.2102, 2013.
- Stensrud, D. J., Bao, J. W., and Warner, T. T.: Using Initial Condition and Model Physics Perturbations in Short-Range Ensemble Simulations of Mesoscale Convective Systems, Mon. Weather Rev., 128, 2077–2107, doi:10.1175/1520-0493(2000)128<2077:UICAMP>2.0.CO;2, 2000.
  - Stephens, G. L.: Radiation Profiles in Extended Water Clouds. II: Parameterization Schemes, J. Atmos. Sci., 35, 2123–2132, doi:10.1175/1520-0469(1978)035<2123:RPIEWC>2.0.CO;2, 1978.
- Suzuki, K., Nakajima, T. Y., and Stephens, G. L.: Particle Growth and Drop Collection Efficiency of Warm Clouds as Inferred from Joint CloudSat and MODIS Observations, J. Atmos. Sci., 67, 3019–3032, doi:10.1175/2010JAS3463.1, 2010.





- Takano, Y., and Liou, K. N.: Solar Radiative Transfer in Cirrus Clouds. Part I: Single-Scattering and Optical Properties of Hexagonal Ice Crystals, J. Atmos. Sci., 46, 3–19, doi:10.1175/1520-0469(1989)046<0003:SRTICC>2.0.CO;2, 1989.
- Thompson, G., Rasmussen, R. M., and Manning, K.: Explicit forecasts of winter precipitation using an improved bulk microphysics scheme. Part I: Description and sensitivity analysis, Mon. Weather Rev., 132, 519–542, doi:10.1175/1520-0493(2004)132%3C0519:EFOWPU%3E2.0.CO;2, 2004.
- Twomey, S.: The Influence of Pollution on the Shortwave Albedo of Clouds, J. Atmos. Sci., 34, 1149–1152, doi:10.1175/1520-0469(1977)034<1149:TIOPOT>2.0.CO;2, 1977.
- Vukicevic, T., Greenwald, T., Zupanski, M., Zupanski, D., Vondar Harr, T., and Jones, A. S.: Mesoscale cloud state estimation from visible and infrared satellite radiance, Mon. Weather Rev., 132, 3066–3077, doi:10.1175/MWR2837.1, 2004
- Wen, Q. S., and Wang, D. H.: Test of GSI-Based Rapid Update Cycle Numerical Prediction in Southern China, Meteorol. Mon., 43, 653–664, doi:10.7519/j.issn.1000-0526.2017.06.002, 2017.
  - Whitaker, J. S., and Hamill T. M.: Ensemble Data Assimilation without Perturbed Observations, Mon. Weather Rev., 130, 1913–1924, doi:10.1175/1520-0493(2002)130<1913:EDAWPO>2.0.CO;2, 2002.
- Winterrath, T. and Rosenow, W.: A new module for the tracking of radar-derived precipitation with model-derived winds, Adv. Geosci., 10, 77–83, doi:10.5194/adgeo-10-77-2007, 2007.
  - Xu, D. M., Huang, L. Z., Min, J. Z., Jiang, L. P., Shen, F. F., and Lei, Y. H.: Impacts of the all-sky assimilation of FY-3D and FY-3E MWHS-2 radiances on analyses and forecasts of Typhoon Muifa (2022), Atmos. Res., 310, 107646, doi:10.1016/j.atmosres.2024.107646, 2024
- Yang, J., Zhang, Z. Q., Wei, C. Y., Lu, F., and Guo, Q.: Introducing the New Generation of Chinese Geostationary Weather Satellites, Fengyun-4, Bull. Amer. Meteor. Soc., 98, 1637–1658, doi:10.1175/BAMS-D-16-0065.1, 2017.
  - Yao, B., Liu, C., Yin, Y., Zhang, P., Min, M., and Han, W.: Radiance-based evaluation of WRF cloud properties over East Asia: Direct comparison with FY-2E observations, J. Geophys. Res. Atmos., 123, 4613–4629. doi:10.1029/2017JD027600, 2018.
- Zhang, S. Q., Zupanski, M., Hou, A. Y., Lin, X., and Cheung, S. H.: Assimilation of Precipitation-Affected Radiances in a
   Cloud-Resolving WRF Ensemble Data Assimilation System, Mon. Weather Rev., 141, 754–772, doi:10.1175/MWR-D-12-00055.1, 2013.
  - Zhou, Y. B., Liu, Y. B., Huo, Z. Y., and Li, Y.: A preliminary evaluation of FY-4A visible radiance data assimilation by the WRF (ARW v4.1.1)/DART (Manhattan release v9.8.0)-RTTOV (v12.3) system for a tropical storm case, Geosci. Model Dev., 15, 7397–7420, doi:10.5194/gmd-15-7397-2022, 2022.
- Zhou, Y. B., Liu, Y. B., and Han, W.: Demonstrating the potential impacts of assimilating FY-4 visible radiances on forecasts of cloud and precipitation with a localized particle filter, Mon. Weather Rev., 151, 1167–1188, doi:10.1175/MWR-D-22-0133.1, 2023.



710



Zhou, Y. B., Cao, T. R., and Zhu, L.: Optimizing cloud optical parameterizations in Radiative Transfer for TOVS (RTTOV v12.3) for data assimilation of satellite visible reflectance data: an assessment using observed and synthetic images, Atmos. Meas. Tech., 18, 3267–3285, doi:10.5194/amt-18-3267-2025, 2025.

Zhu, Y. Q., Liu, E., Mahajan, R., Thomas, C., Groff, D., Van Delst, P., Collard, A., Kleist, D., Treadon, R., and Derber, C. J.: All-Sky Microwave Radiance Assimilation in NCEP's GSI Analysis System, Mon. Weather Rev., 144, 4709–4735, doi:10.1175/MWR-D-15-0445.1, 2016.